The Pennsylvania State University

The Graduate School

Department of Aerospace Engineering

MODELING WIND TURBINE / TOWER INTERACTIONS WITHIN AN ACTUATOR LINE MODEL

A Thesis in

Aerospace Engineering

by

Zhixiang Wang

Submitted in Partial Fulfillment
of the Requirements
for the Degree of

Master of Science

August 2015

The thesis of Zhixiang Wang was reviewed and approved* by the following:

Sven Schmitz
Assistant Professor of Aerospace Engineering
Thesis Advisor

Mark D. Maughmer
Professor of Aerospace Engineering

George A. Lesieutre
Professor of Aerospace Engineering
Head of the Department of Department or Graduate Program

*Signatures are on file in the Graduate School

ABSTRACT

The wind turbine tower causes time-varying turbine blade loads and wake behavior; however, the interactions of the turbine blades with the tower are not accounted for in state-of-the-art computational fluid dynamic simulations of wind plants. In this thesis, a tower model is developed using the body-force method, specifically, the actuator line method. The actuator line method has been widely used to model wind turbine rotors in flow simulations of wind plants. The tower model is implemented into the full-scale NREL Phase VI turbine simulation under uniform inflow and steady yaw conditions. The simulation results, primarily the blade loads predictions along the turbine blades, are compared to wind tunnel test data from the NREL Phase VI Unsteady Aerodynamics Experiment. Quantitative comparisons against measured NREL data were performed for both spanwise and phase-averaged sectional blade loads as a function of rotor azimuth. The proposed tower model is well validated and be easily implemented by the wind energy community for use in both actuator line wind plant simulations and other fully blade-resolved wind turbine simulations.

TABLE OF CONTENTS

LIST OF FIGURES

LIST OF TABLES

ACKNOWLEDGEMENTS

This thesis would not have been possible without the support of many people. Many thanks to my academic advisor, Dr. Sven Schmitz, who gave me many useful suggestions during the thesis work and final paper revisions. Also, many thanks to Dr. Matthew J. Churchfield from NREL for guidance on the OpenFOAM flow simulations. Many thanks are also directed towards Dr. Scott Schreck from NREL for providing validation data sets of the NREL Phase VI rotor experiment. I also would like to thank Mr. Kirk Heller for technical support with the Department of Aerospace Engineering computing clusters. Finally, many thanks to my parents who supported my graduate study and numerous friends who always offered me great support and love.

Chapter 1 Introduction

Mankind has a long history of using wind as an energy source. Particularly, windmills were created to utilize the wind resource for mechanical work and production such as grinding grain and pumping water for irrigation. After people started using electricity for lighting, the windmill's mission shifted to electricity production with the first one built in 1887 [1]. Later on, wind energy has become an essential source for electricity; meanwhile, the design method and philosophy of wind turbines have become increasingly sophisticated.

1.1 Wind Turbine Design

Early in the windmill history, the design of windmills relied mainly on previous experience. In 1880, John Smeaton became the first one to study and evaluate scientifically the performance of the wind turbine [2]. One of his findings was that the maximum power of a wind turbine is proportional to the cube of the incoming wind speed. This characteristic makes the wind resource very valuable in producing power because a doubled wind speed returns eight times the amount of the power. The extensive usage of wind turbines for electrical power production drives the modern wind turbine design. During the 20th century, small wind stations as well as large utility-scale wind generators were designed and developed. Especially, for large utility-scale wind turbines, the size and rated power scale are increasing very quickly as shown in Figure 1-1. The rotor diameter has already reached the scale of a large commercial aircraft wingspan, and a typical turbine blade planform has a complex shape with both taper and twist.

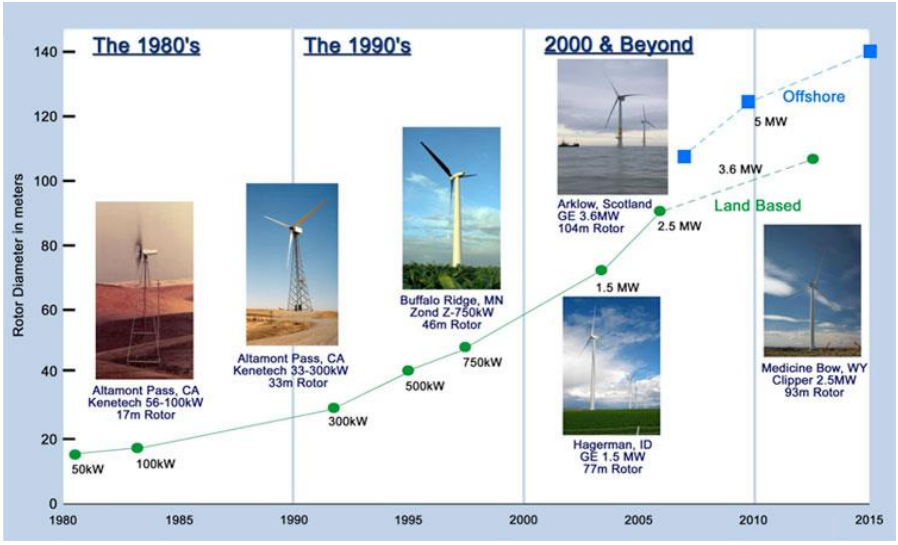

Figure 1-1. Evolution of U.S. Commercial Wind Scale [3].

1.2 Wind Turbine Aerodynamic Modeling

The application of advanced aerodynamics plays an important role in the evolution of wind turbine design methods, and it continuously shapes the geometry of wind turbines and optimizes its power performance. Poul la Cour of Denmark built the first wind turbine (Figure1-2) based on aerodynamic design principles [4]. It had lower solidity but higher rotation speed than previous wind turbines. The gain of such a design was that it operates closer to the optimum tip speed ratio suggested earlier by Smeaton. Contrary to modern wind turbine design, which has a rather small tip chord, he believed the blade should have higher solidity at the tip. This is only true, though, if there is no tip vortex and resulting rotational effects.

To understand the principle of wind turbine aerodynamics, it is important to first identify the flow field around the wind turbine. From the prospective of the wind turbine, the turbine blade rotates around its axis, so the speed varies along the span, and thus each blade section has a different inflow condition with axial and angular induction. From the point-of-view of the surrounding environment, there exists wind gust in the atmospheric boundary layer, which makes the inflow

condition much more complex. Hence the whole system is time-varying and strongly three-dimensional. To reduce the complexity and derive fundamental theories for wind turbine aerodynamics, some assumptions and simplifications are needed.

Figure 1-2. La Cour's windmill [5].

The most classical wind turbine aerodynamic model is that of the actuator disk model. The air is assumed to be steady, 1-D, inviscid, and irrotational. The operation of the wind turbine is treated as a momentum extraction and energy-harvesting process. The streamtube analysis of the actuator disk model is shown in Figure 1-3. From the actuator disk model, we know there exists an ideal upper limit for the power coefficient of $Cp_{max} \approx 0.59$, known as the "Betz Limit".

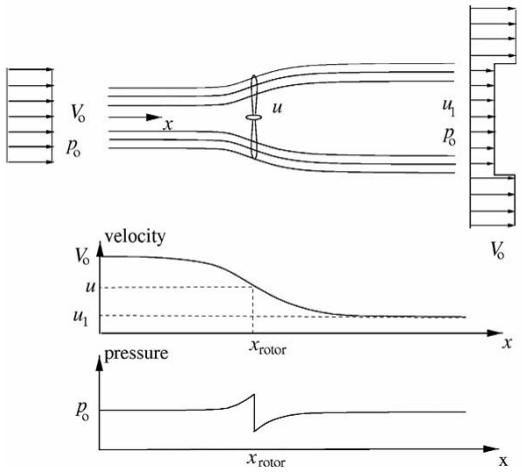

Figure 1-3. Streamtube analysis of pressure and axial velocity in the actuator disk model [6].

An improved model named the rotor disk model further considers the rotation of the rotor disk and wake (Figure 1-4). The maximum power coefficient, taking wake rotation into account, is shown in Figure 1-5. The tip speed ratio is defined as $\lambda = \Omega R / V_0$ where Ω is the rotation rate of the rotor, R is the radius of the blade, and V_0 is the upstream wind speed.

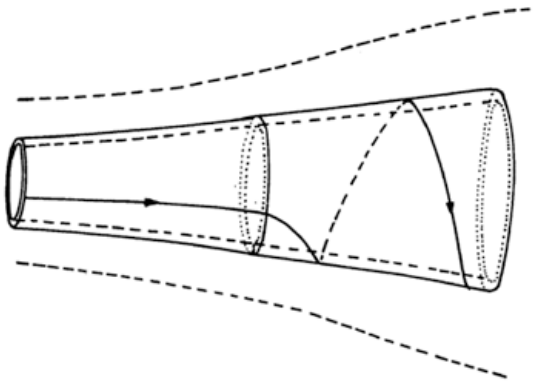

Figure 1-4. Streamtube model for rotor disk model [7].

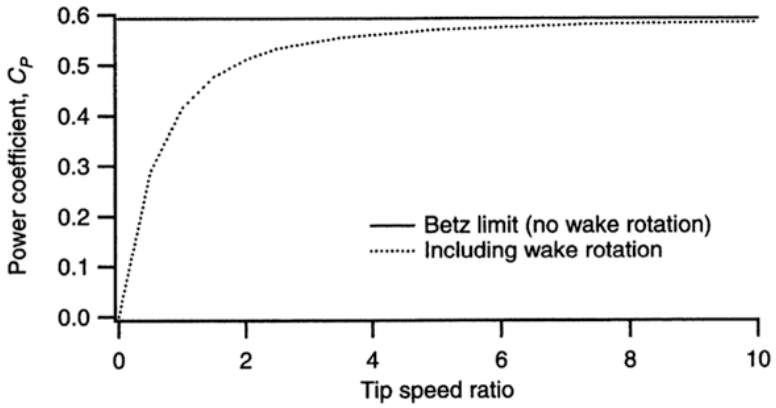

Figure 1-5. Maximum power coefficient vs. tip speed ratio considering wake rotation [8].

The deficiency of the above two models is that they do not account for the flow details near the blade. A more advanced model, called Blade Element Momentum (BEM) theory extends the 1-D assumption to 2-D, while accounting for 3-D effects by applying root and tip loss correction factors. In BEM theory, the inflow details at each blade section are studied, with the incremental torque and thrust determined (Figure1-6) by analyzing the local flow angle, ϕ, and using airfoil tables

available from wind tunnel tests or theory. At present, the BEM method is still widely used in wind turbine design and analysis.

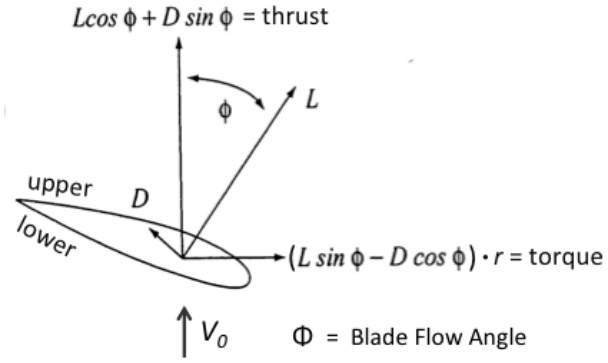

Figure 1-6. Incremental torque and thrust at a section of blade in BEM theory.

Computational fluids dynamics (CFD) has gained popularity in wind turbine design and analysis by resolving flow physics in a high-fidelity model environment. But it is also quite computationally expensive and requires a complex rotating mesh near the turbine blade to fully resolve the flow in the blade boundary layer. Today, the wind energy community commonly cares increasingly about analyzing the operation of a large wind farm rather than a single turbine. Using CFD, the range of scales goes from a millimeter in the blade boundary layer to kilometers for the mesoscale (weather). A full computation across all scales is not feasible. New computational methods include hybrid CFD methods, which couple the near-blade CFD with vortex-wake methods [9]. For wake modeling methods, the rotating, resolved near-blade mesh is not needed around the blade, which greatly reduces the computational cost. Although the reduced complexity is achieved at an expense of flow details near the turbine blade and wake, it has fidelity in producing the blade tip and root vortices and is capable of constructing an accurate far-field wake. This makes this approach scalable for large wind farm simulations.

1.3 Modeling Tower Effect

In the previous discussion of wind-turbine aerodynamic model analysis, it should be noted that the tower was not included, and its effect on the turbine rotor is also not considered. The tower itself generates a deficit in the flow velocity and small-scale turbulence in the downstream flow. When the blade passes through this azimuthal region, each blade-section inflow conditions are changed, and thus the aerodynamic forces acting on the blade are altered. This is known as blade-tower interaction. In reality, the tower effect plays an important role in the turbine wake structure and also blade fatigue. The former influence, though, is a minor effect for a single wind turbine, but is significant for a large wind farm because the wake will affect the performance of the turbines downstream; the latter influence, as a 1-per-rev dynamic loading along the span, is quite important for structural health of large utility-scale wind turbines.

The majority of wind turbines are horizontal-axis wind turbines (HAWT), and they can be further divided into two groups, the downwind type, if the tower is upstream of the turbine rotor, and the upwind type, if the rotor is upstream of the tower (Figure 1-7). The mechanism of a tower effect is different for the upwind-type turbine and downwind-type turbine. For the upwind configuration, the mechanism is quite simple. It is mainly a result of deflection of the flow upstream of the tower [10]. Apparently, the strength of this effect is strongly affected by the distance between the rotor disk and the tower and can be negligible, if this distance is much larger than the tower cross-section diameter. For a downwind turbine configuration, this interaction is usually called “tower shadow”. The blade directly interacts with the tower wake, which contains more flow variability than the flow upstream. In the tower wake, the flow speed is reduced and turbulence is generated along with vortex shedding induced by the tower flow separation off the tower. Experience shows that 30% wind speed is lost after the wind passes the tower space [11], which is a significant wake deficit.

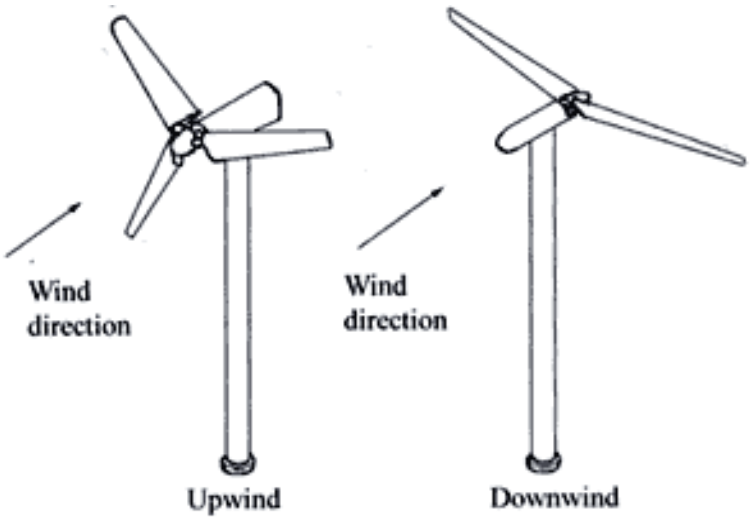

Figure 1-7. Upwind turbine configuration and downwind turbine configuration [12].

There are many ways to model the tower in CFD simulations. The most common way is to use a body-fitted conformal mesh around the tower. As discussed previously, this approach provides high fidelity at an expense of complex grid generation and computational cost. Another way is the immersed-boundary method, a review of which can be found in [13]. It is compatible with the Cartesian grid, which reduces the work on mesh generation, but modifications are needed for the pressure and velocity at the near-wall points (or cells) to satisfy the boundary condition. A third approach is the body-force method as discussed in the rotor model. It works with any type of grid and is easy to implement into the solver. Though it sacrifices the fidelity in flow detail of the near wake, it provides a good representation in the far wake, which is important in large wind farm simulations. Since the tower is stationary in the physical domain and has a rather simple geometry, it is possible to improve its near-field performance by adding a bit of complexity to the body-force model using the knowledge from the flow over a cylinder at representative Reynolds numbers. Adding such a tower model will not dramatically increase the computational time and cost compared to a single turbine simulation.

In this thesis, several tower models are proposed using the body-force method. They are applied to a NREL Phase VI rotor simulation using the computational solvers OpenFOAM. The reasons

for choosing the NREL Phase VI rotor are that 1) It is a wind turbine, which has been extensively tested and used for scientific research. The tower geometry is well documented. The underlying NREL Phase VI Unsteady Aerodynamics Experiment provides detailed blade-load measurements for a range of wind speeds and steady yaw angles. The phase-averaged blade load measurements can be used to validate the performance of the tower model. 2) The NREL Phase VI rotor is an upwind-type turbine, which has a simpler tower effect and mechanism compared with the downwind type. In addition, it represents blade-tower interactions in modern wind farms. 3) The turbine rotor model for the NREL Phase VI rotor, using the body force-method, has already been developed and examined in previous work [14].

1.4 Thesis Outline

In the second chapter, the CFD method used in this study is introduced with the platform and flow solver, OpenFOAM. Following that, the rotor blade representation using a body-force method as an actuator-line is presented. The third chapter presents the foundation of the tower models. It starts with a review of studies on flow over circular cylinder, briefly discusses the analytical solution to cylinder flow from potential theory, and summarizes the results of the experimental studies on circular cylinder flow. This chapter ends with proposing three types of tower models that are implemented and analyzed in the simulations. In the fourth chapter, the results of the LES simulation of a single NREL Phase VI rotor operating in uniform wind speed and steady yaw angle, are presented as validation data for the tower model. The aerodynamic loads along the turbine blades at compared with measured data of the NREL Phase VI experiment. To explore the generality of the model, comparisons are made that includes different wind speeds and different yaw angles. In the last chapter, some conclusions are drawn with some ideas for future work.

Chapter 2 Numerical Methods

In this section, the methods for the wind-turbine tower-model study are presented. It is a hybrid CFD approach using Large Eddy Simulation (LES) and a body-force method. The flow solver and scheme are discussed first, then the concept of the actuator line method is presented to model the turbine rotor. In addition, a review of theoretical and experimental studies of cylinder flow is presented, followed by the development of the tower model using the body-force method.

2.1 Flow Solver

The LES solver used in this study computes the incompressible filtered Navier-Strokes equations built on the Open Field Operation and Manipulation (OpenFOAM) CFD Toolbox, an open-source CFD software package used to solve partial differential equations [15]. The governing equations are solved using the unstructured finite-volume formulation with second-order Crank-Nicolson scheme in time integration, and a blending of central differencing and upwind differencing for the spatial discretization. The solver is a modified version of pisoFoam, a standard OpenFOAM solver. The external body-force term is added to accommodate the actuator model for the rotor and tower. The code is parallelized using the message-passing interface (MPI). Time advancement uses Issa's [16] predictor-corrector pressure-implicit splitting operation (PISO) with one predictor followed by three correctors. The momentum equation is solved using a Poisson equation for the pressure, as done in classical pressure-correction methods. To avoid the pressure-velocity decoupling, the velocity-flux interpolation at the cell faces follows that of Rhie-Chow [17]. Other interpolation from cell centers to faces is a mix of linear (second-order central differencing) with a small amount of first-order upwinding. In this study, upstream to the tower, a blend of 20% first-order upwind and 80% central differencing is used to remove numerical oscillations caused by the rotor's and

tower's body-force model. Downstream of the tower, a mix of 2% upwind and 98% central differencing is used to minimize artificial wake dissipation. More details about the solver can be found in Churchfield et al. [18].

2.2 Actuator Line Method

The actuator-type aerodynamic method, as stated in the previous chapter, is a compromise between the low-fidelity engineering model and a high-fidelity fully blade-resolved CFD method. The first-order type of actuator methods is the rotor disk model, which uses a disk of azimuthally-averaged body force to replace the rotor. The body force is treated as an external force term in the momentum equation of the flow solver [19]. As a rotor disk model, it neither accounts for the details of the rotor blade, nor does it capture the blade tip and root vortices.

The next level of actuator-type methods is the actuator line method (ALM). In the ALM, the turbine blade is modeled by a number of discrete actuator points along the blade lifting line that rotates in the flow field. The forces at each actuator point are projected onto the flow field as a volume force. Mathematically, these volume forces are also treated as an external force term added to the momentum equation at respective grid points. These volume forces are indeed the sectional lift and drag forces acting on the turbine blades. The magnitude of the forces are found following the same process as in Blade Element Momentum (BEM) theory. The local velocity triangle is first determined by the local velocity vector, $\boldsymbol{V_{rel}}$, and total blade twist angle, β, at each actuator point (Figure 2-1). Then the lift coefficient, C_l, and drag coefficient, C_d, are found from airfoil tables. Finally, the magnitude of the forces is calculated by

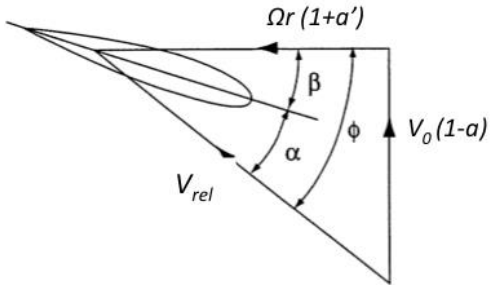

Figure 2-1. Blade section local velocity triangle [20].

$$L = \frac{1}{2} C_l \rho V_{rel}^2 c \Delta d \tag{2-1}$$

$$D = \frac{1}{2} C_d \rho V_{rel}^2 c \Delta d \tag{2-2}$$

where c is the local chord length and Δd is the incremental blade section span, i.e. the distance between two adjacent actuator points. In general, airfoil tables are obtained from steady wind tunnel tests and do not account for 3-D effects along the rotating blade such as centrifugal pumping effect and stall delay. This can be partially accounted for by coupling the airfoil table with 3-D correction methods such as the AirfoilPrep software developed by NREL [21]. Since the flow field is resolved three-dimensionally, there is no need to applying a root or tip loss factor as done in BEM; the root and tip vortices are captured by the solver. A schematic of the ALM is shown in the Figure 2-2.

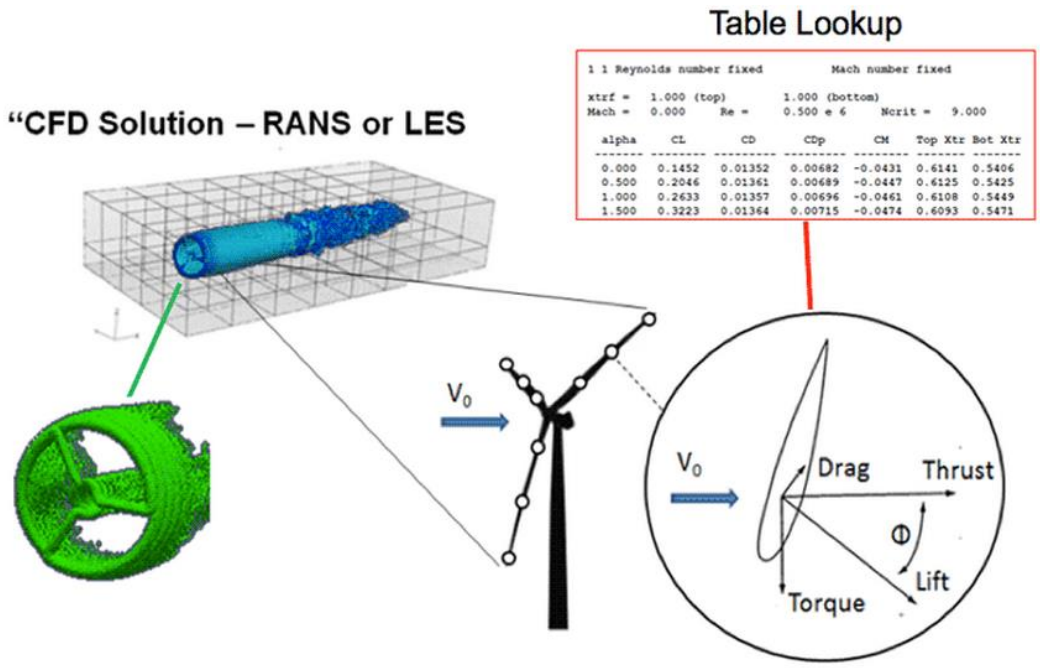

Figure 2-2. Overview of actuator line method [22].

2.2 Actuator Line Method – Rotor Model

The turbine-rotor actuator line model within the ALM follows that of Sørensen and Shen [23]. The rotor blades are represented by rotating actuator lines, and each line is discretized into a number of actuator points. The velocity vector is sampled at the center of each actuator point, which is also the center of the bound vortex. The lift and drag forces generated at each actuator point are projected as volume forces and included in the momentum equation. The aerodynamic force vector at blade element, *j*, located at $\left(x_j, y_j, z_j\right)$ at time *t* is $f_i^A\left(x_j, y_j, z_j, t\right)$. The projected force vector at a location $\left(x, y, z\right)$ at time *t*, due to the aerodynamic forces of all blade elements is

$$F_i^A(x,y,z,t) = \sum_{j=1}^{N} f_i^A\left(x_j, y_j, z_j, t\right) \frac{1}{\varepsilon^3 \pi^{3/2}} \left[-\left(\frac{|\mathbf{r}|}{\varepsilon} \right)^2 \right] \tag{2-3}$$

where ε is the Gaussian spreading width, which controls the projection width and peak magnitude and **r** is the vector from actuator element, *j*, located at (x_j, y_j, z_j) to point (x, y, z) in the flow field.

The Gaussian spreading width, ε, at each actuator point is determined following the elliptical distribution concept proposed by Jha et al. [24]. It is hypothesized that the Gaussian spreading width, ε, should be proportional to the actual magnitude of the sectional blade force rather than the blade planform. The process of finding the Gaussian spreading width is as follows:

1) Find the blade aspect ratio **AR**

$$\bar{c} = \frac{1}{R}\int_0^R c(r)dr \tag{2-4}$$

$$AR = \frac{R}{\bar{c}} \tag{2-5}$$

2) Find a 'fictitious' elliptic planform with the same **AR**

3) Assume that

$$c_0 = \frac{4}{\pi}\bar{c} \tag{2-6}$$

$$c^*(r) = c_0\sqrt{1-(\frac{2r}{R})^2} \tag{2-7}$$

$$\varepsilon(r) / c^*(r) = \varepsilon_0 / c_0 = \text{const} \tag{2-8}$$

$$\varepsilon_0 = n_{\max}\Delta r \tag{2-9}$$

$$\varepsilon_{R/2} = n_{\min}\Delta r \tag{2-10}$$

with n_{min} = 1 as a minimum discretization threshold on any given grid. n_{min} need not be an integer. Also,

$$n_{\max} = \frac{\Delta r}{R} \approx 0.08...0.10 \tag{2-11}$$

where Δr is the local grid size, n_{min} and n_{max} are used to constrain the minimum and maximum Gaussian spreading width, ε. Combining the equations above, the expression for the Gaussian spreading width becomes

$$\varepsilon / c^* = \frac{\Delta r}{4R} n_{\max}(\pi \mathbf{AR}) = const \ . \tag{2-12}$$

2.3 Unsteady Aerodynamics Experiment

A comprehensive test program, the Unsteady Aerodynamics Experiment (UAE), was conducted by the National Renewable Energy Laboratory (NREL) [25]. The test aimed at gaining knowledge of turbine behavior under various conditions such as steady yaw and tower shadow. The lack of data knowledge and quantification constrained the experts' modeling tool and made the modeling quality rely on the modeler's skill and experience. Early tests were accomplished as field tests at the National Wind Technology Center (NWTC) with a 10m diameter, horizontal-axis research wind turbine. It was concluded that the outdoor operation was much too complex for model tool validation.

A new set of full-scale tests was designed and conducted in the NASA-Ames 24.4m by 36.6m wind tunnel [26]. The goal of this test was to have accurate quantitative aerodynamic and structural measurements on a wind turbine under controlled conditions. An overview of all the test sequences is shown in Figure 2-3. Some tests aimed at emulating field operation, while most focused on collecting data to study specific flow phenomena. The test sequence used in this study is Sequence S. The NREL Phase VI rotor is an upwind, rigid turbine (Figure 2-4(a)); its tower geometry is shown in Figure 2-4(b). The NREL Phase VI rotor has two blades equipped with the S809 airfoil and is stall regulated. The blade geometry is shown in Figure 2-5. Measurements of blade surface

pressures, angle of attack, and inflow dynamic pressure at five span locations, i.e. 30%, 47%, 65%, 80%, and 95% were performed. Turbine yaw angle was precisely controlled by a servo.

Table 1. Test Matrix Overview

Ordinal Number	Test Sequence	Upwind/ Downwind	Rigid/ Teetered	Cone Angle (deg)	Yaw Angle (deg)	Slow Yaw Sweep	Blade Tip Pitch (deg)	Parked/ Rotating	RPM	Blade Press.	Probe Press.	Blade Tip	Day	NASA Run Number
B	Downwind Baseline (F)	Downwind	Teetered	3.4	Locked		3.0	Rotating	72.0	X	X	Baseline	1-4	11-14
C	Downwind Low Pitch (F)	Downwind	Teetered	3.4	Locked		0.0	Rotating	72.0	X	X	Baseline	1-4	11-14
D	Downwind High Pitch (F)	Downwind	Teetered	3.4	Locked		6.0	Rotating	72.0	X	X	Baseline	1-4	11-14
E	Yaw Releases (P)	Downwind	Rigid	3.4	Locked / Free		3.0	Rotating	72.0	X	X	Baseline	5	15, 16
F	Downwind High Cone (F)	Downwind	Rigid	18.0	Locked		3.0	Rotating	72.0	X	X	Baseline	6	17
G	Upwind Teetered (F)	Upwind	Teetered	0.0	Locked		3.0	Rotating	72.0	X	X	Baseline	8-9	34, 38
H	Upwind Baseline (F)	Upwind	Rigid	0.0	Locked	X	3.0	Rotating	72.0	X	X	Baseline	9,11,12,15	39, 41-43, 50
I	Upwind Low Pitch (F)	Upwind	Rigid	0.0	Locked	X	0.0	Rotating	72.0	X	X	Baseline	9,11,12	39, 41-43
J	Upwind High Pitch (F)	Upwind	Rigid	0.0	Locked	X	6.0	Rotating	72.0	X	X	Baseline	9,11,12	39, 41-43
K	Step AOA, Probes (P)	Upwind	Rigid	0.0	Locked at 0		Step & ramp	Rotating	72.0	X	X	Baseline	15	50
L	Step AOA, Parked (P)	Upwind	Rigid	0.0	Locked at 0		Step & ramp	Parked	0.0	X	X	Baseline	13	48
M	Transition Fixed (P)	Upwind	Rigid	0.0	Locked	X	3.0	Rotating	72.0	X		Baseline	16	52
N	Sin AOA, Rotating (P)	Upwind	Rigid	0.0	Locked at 0		Sinusoidal	Rotating	72.0	X	X	Baseline	14,15	49, 50
O	Sin AOA, Parked (P)	Upwind	Rigid	0.0	Locked at 0		Sinusoidal	Parked	0.0	X	X	Baseline	13	44-47
P	Wake Flow Vis. Upwind (P)	Upwind	Rigid	0.0	Locked		3.0, 12.0	Rotating	72.0			Visualize	10,11	40, 41
Q	Dynamic Inflow (P)	Upwind	Rigid	0.0	Locked at 0		Step	Rotating	72.0	X	X	Baseline	15	50
R	Step AOA, No Probes (P)	Upwind	Rigid	0.0	Locked at 0		Step & ramp	Rotating	72.0	X		Baseline	16	52
S	Upwind, No Probes (F)	Upwind	Rigid	0.0	Locked	X	3.0	Rotating	72.0	X		Baseline	16,18	52, 54
T	Upwind, 2 deg Pitch (F)	Upwind	Rigid	0.0	Locked at 0		2.0	Rotating	72.0	X		Baseline	16,18	52, 54
U	Upwind, 4 deg Pitch (F)	Upwind	Rigid	0.0	Locked at 0		4.0	Rotating	72.0	X		Baseline	16,18	52, 54
V	Tip Plate (F)	Upwind	Rigid	0.0	Locked at 0		3.0	Rotating	72.0	X		Plate	18	54
W	Extended Blade (F)	Upwind	Rigid	0.0	Locked at 0		3.0	Rotating	72.0	X		Extended	18	54
X	Elevated RPM (F)	Upwind	Rigid	0.0	Locked at 0		3.0	Rotating	90.0	X		Baseline	19	55
3	Tower Wake Measure (P)	Downwind	Rigid	3.4	Locked		53-79	Parked	0.0	X	X	Baseline	6	18
4	Static Press. Cal (P)	Downwind	Teetered	3.4	Locked at 0		3.0	Rotating	72.0	X	X	Baseline	4	14
5	Sweep Wind Speed (F,P)	Upwind	Rigid	0.0	Locked		3.0, 6.0	Rotating	72.0	X	Both	Baseline	11,19	43, 55
6	Shroud Wake Measure (P)	Downwind	Rigid	3.4	Locked		61-74	Parked	0.0	X	X	Baseline	7	19
7	Shroud Operating (P)	Downwind	Rigid	3.4	Locked		3.0	Rotating	72.0	X	X	Baseline	7	20
8	Downwind Sonics (F,P)	Upwind	Rigid	0.0	Locked		3.0	Rotating	72.0	X		Baseline	17	53
9	Sonic Validation (P)	Upwind	Rigid	0.0	Locked		3.0	Rotating	72.0			Baseline	17	53

(F) - Test conditions representative of field operation

(P) - Test conditions designed to explore specific flow physics phenomena

Figure 2-3. Overview of all test cases (Unsteady Aerodynamics Experiment, NREL Phase VI Rotor) [25].

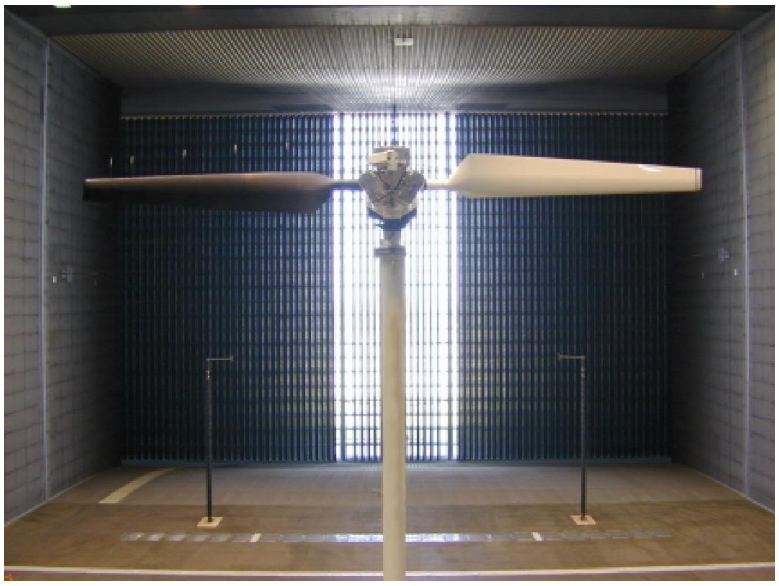

(a)

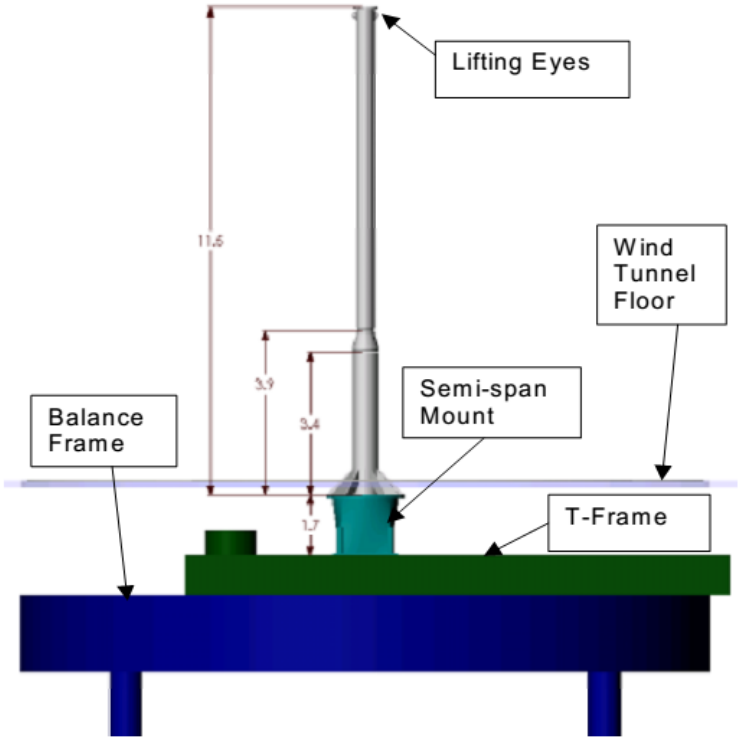

(b)

Figure 2-4. (a) NREL Phase VI wind turbine (b) NREL Phase VI wind turbine tower [26].

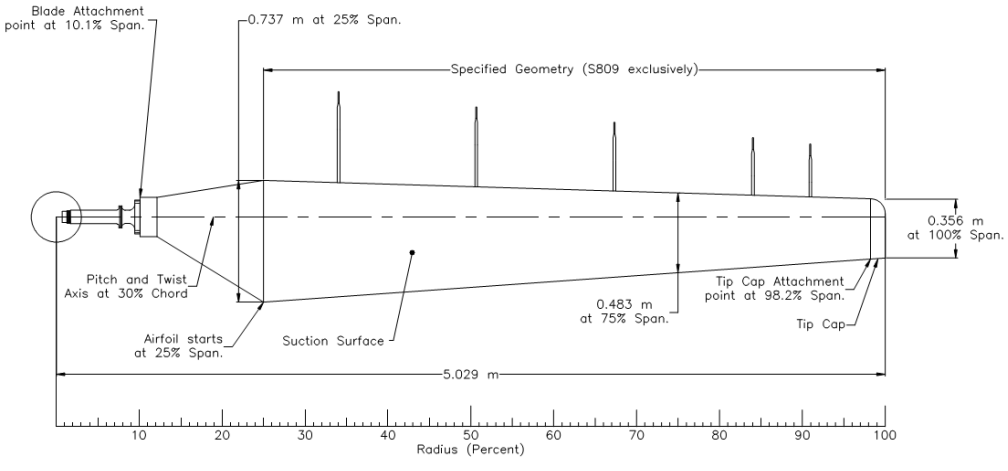

Figure 2-5. NREL Phase VI rotor blade geometry [26].

In test sequence S, wind speeds ranged from 5m/s to 25m/s, and yaw angles ranged from 0° to 180°. Table 2-1 gives an overview of the flow conditions considered in this work, and Table 2-2 shows the Reynolds number with respect to the tower diameter at each wind speed.

Table 2-1. Summary of flow conditions for simulations of NREL Phase VI Rotor.

Yaw angle / Wind speed (m/s)	0º	10 º	20 º
5	×	×	
7	×	×	×
9	×	×	

Table 2-2. Tower Reynolds number at different wind speed (NREL Phase VI Rotor).

Wind speed (m/s)	Re_D
5	1.11×10^5
7	1.56×10^5
9	2.00×10^5

2.4 Cylinder Flow

To develop the tower model using the body-force method, a basic knowledge of cylinder flow is reviewed in this section. Cylinder flow is one of the most fundamental flows in fluid mechanics. Neglecting viscous effects, a well-known analytic solution has been derived from potential-flow theory with the absence of flow separation. The flow speed recovers to its upstream value at the rear part of the circular cylinder. Using cylindrical coordinates, the stream function for the non-rotating circular cylinder flow is

$$\psi = U_\infty r(1-\frac{a^2}{r^2})\sin\theta \tag{2-13}$$

where a is the radius of the cylinder, r is the radial coordinate, and θ is the azimuth angle. The normal and tangential velocities along the surface of the cylinder are found as

$$v_{rs} = 0 \tag{2-14}$$

$$v_{\theta s} = -2U_\infty \sin\theta \ . \tag{2-15}$$

The pressure distribution along the cylinder surface can be expressed as

$$p_s = p_\infty + \frac{1}{2}\rho U_\infty^2(1-4\sin^2\theta) \tag{2-16}$$

Accordingly, the pressure coefficient *Cp* becomes

$$C_p = 1-4\sin^2\theta \ . \tag{2-17}$$

Attached is plotted as a function of the azimuth angle in Figure 2-6.

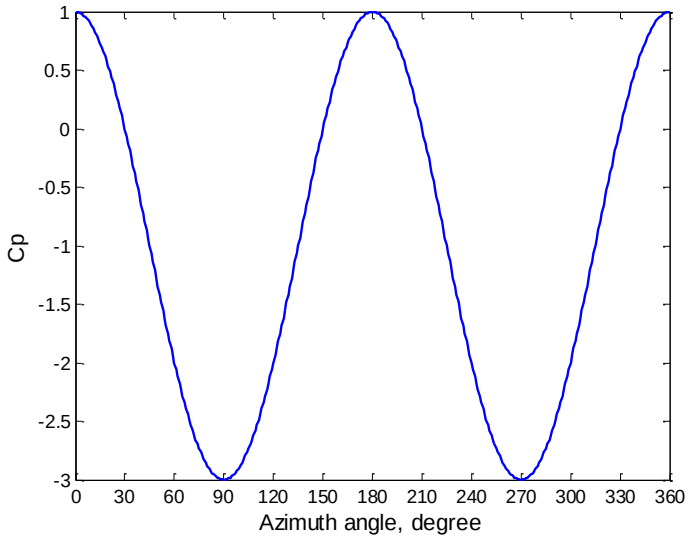

Figure 2-6. Cp distribution along a non-rotating circular cylinder.

In reality, the cylinder flow is much more complex than the result obtained using potential theory. The flow phenomenon has a strong dependence on the Reynolds number. The Reynolds number is

a dimensionless parameter that is related to the ratio of inertial forces to viscous forces and is defined by

$$\mathrm{Re} = \frac{U_\infty L}{\upsilon} \tag{2-18}$$

where U_∞ is the velocity of the object relative to the fluid, L is a characteristic length, and v is the kinematic viscosity of the fluid. Numerous experimental studies have been conducted on cylinder flow. These studies can be divided into two categories, i) those directed at the steady-state properties such as drag coefficient and static pressure, and ii) those concerned with the dynamic properties such as unsteady vortex shedding and separation [27]. For the steady-state phenomena, a number of wind tunnel tests were performed at different Reynolds numbers [28]-[29]. These experimental results define three major regimes in non-rotating circular cylinder flow. The first is the subcritical regime for a Reynolds numbers varying approximately from 10^3 to approximately 3×10^5. The drag coefficient of the circular cylinder varies between 1.0 and 1.2. Laminar-turbulent transition occurs at a Reynolds number of about 3×10^5 where the mean drag coefficient drops to approximately 0.2-0.35, as shown in Figure 2-7. Then, the flow enters the "supercritical" regime. When the Reynolds number is raised to about 3×10^6, the mean drag coefficient increases again to 0.4 up to 0.7. The last regime above this Reynolds number is recognized as "the transcritical" regime. The root-mean-square variation of circular cylinder drag coefficient at different Reynolds number is shown in the Figure 2-8. The drag coefficient variation is about 10% for Reynolds numbers around 10^5, so it is sufficient most of the time to use the steady mean drag coefficient to represent the drag characteristic of the circular cylinder.

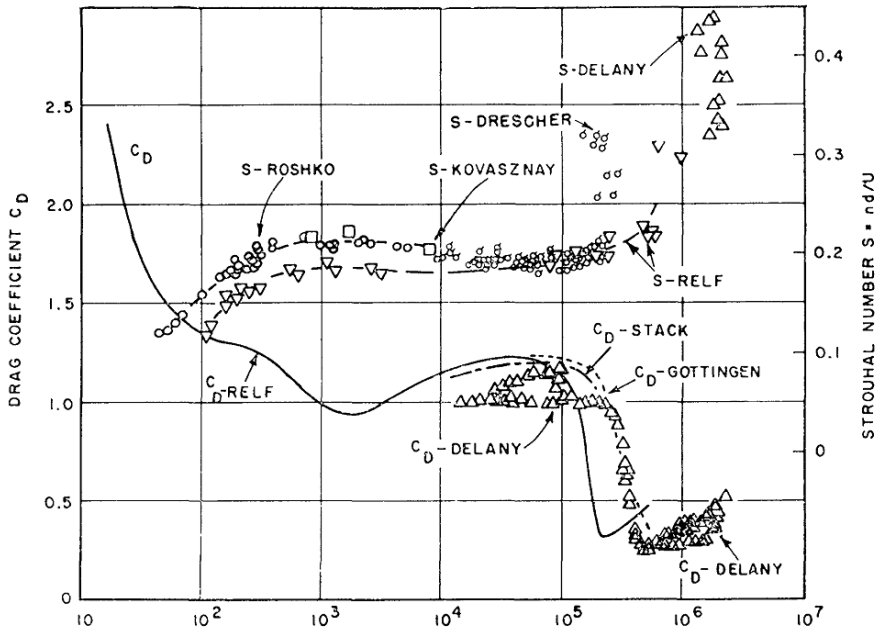

Figure 2-7. Drag coefficient and Strouhal number of a non-rotating circular cylinder as a function of Reynolds number [32].

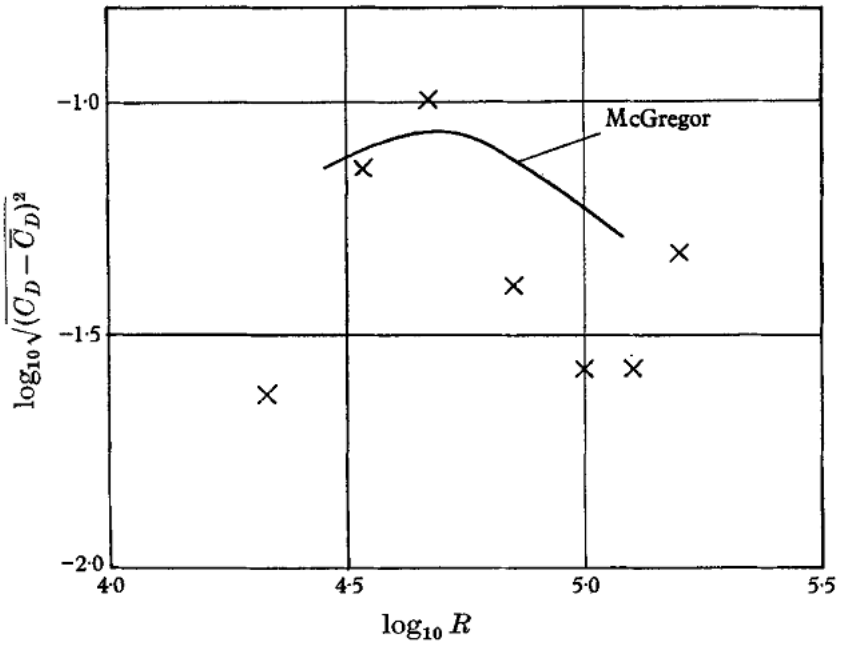

Figure 2-8. Root-mean-square variation of drag coefficient for non-rotating circular cylinder [30].

The mean pressure distribution around the circular cylinder is a reflection of separation. A sample pressure distribution at different Reynolds numbers is shown in Figure 2-9.

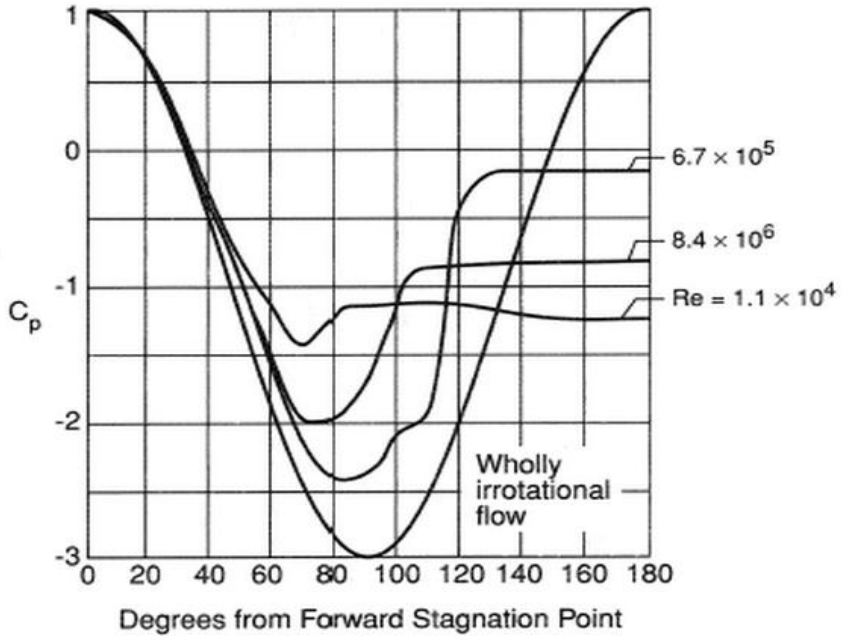

Figure 2-9. Cp distribution along a non-rotating circular cylinder as a function of Reynold number [31].

Unsteady flow phenomena such as vortex shedding and the wake of a tower flow (or cylinder) are also of importance. A dimensionless parameter called Strouhal number can be used to describe the dimensionless frequency of flow shedding. The Strouhal number is defined as

$$St = \frac{fL}{U_\infty} \tag{2-19}$$

where L is the characteristic length (here the tower diameter), U_∞ is the flow velocity, and f is the vortex shedding frequency.

Figure 2-7 also shows the mean drag coefficient and Strouhal number variation as a function of Reynolds number. Experimental results show that the periodicity starts at St = 0.12 at a Reynolds number of about 50. It rises to 0.2 at a Reynolds number of about 300. In the Reynolds number range between 300 and 100,000, it has been verified by Roshko, Kovasznay, and Relf [33] that $St \approx 0.2$. After transition, for higher Reynolds numbers, experiments shows the periodicity does have a single appearance, and the dominant frequencies vary substantially. For example, Relf [34] found

the most prominent disturbance in the Reynolds number range between 10^5 to 10^6 where the Strouhal number raises from 0.2 to 0.3.

2.5 Tower Modeling

Following the review of non-rotating circular cylinder flow, the idea of a tower model using the body-force method is presented in this section. The simplest model is that of a single actuator drag line model, which simply introduces the overall drag effect into the flow field to create a momentum deficit. The second model is named multiple actuator lines model with drag and side forces. Instead of using one actuator line to produce the drag force, multiple actuator lines are used together to model the tower, projecting side forces in addition to the drag force into the flow field. In the end, an advanced actuator-line method, termed the actuator line with Cp-based force distribution model is introduced. It projects the force normal to the cylinder surface with a force distribution related to the mean pressure coefficient *Cp* around the tower (or cylinder). Figure 2-10 shows a diagram of these three different types of tower models. The straight black line represents the tower, while the arrows show the direction of the body force acting on the fluid with its length indicating the strength of the forces.

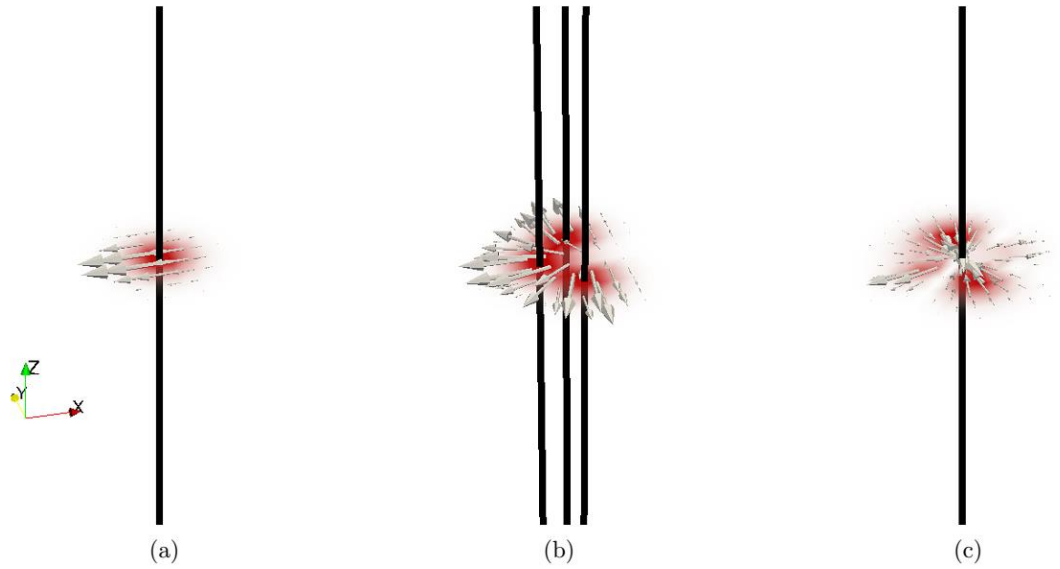

Figure 2-10. Schematic diagram of the different body-force representations of a wind turbine tower (a) Single actuator drag line model, (b) Multiple actuator lines with drag and side forces, (c) Actuator line with Cp-based force distribution model [35].

2.5.1 Single Actuator Drag Line Model

As the most straightforward way to model the tower with a body-force method, the single actuator drag line model only has a drag force. This approach is similar to that of Aitken et al. [36] and Wu and Porté-Agel [37]. The velocity is sampled at the center of each actuator point. Then the drag force is determined by the drag coefficient, C_d, which is chosen from a table lookup of experimental results as discussed in the previous section. Finally, the drag force is projected as a volume force at each actuator point of the drag (actuator) line onto the flow field with a three-dimensional Gaussian function. The projection function is given by

$$g(r) = \frac{1}{\varepsilon^3 \pi^{3/2}} \exp[-(r/\varepsilon)^2] \tag{2-20}$$

where r is distance between the actuator-point center and the force-projection point. The parameter ε is the Gaussian projection width. The tower essentially works as a parked rotor blade with no lift. Two parameters can be varied for this model, one is the drag coefficient, C_d, and another is the

Gaussian projection width, ε. The choice of the Gaussian projection width, ε, is chosen based on the tower diameter, D.

The weakness of the single actuator drag line model is that it transfers limited information about the tower effect into the flow field. For example, the flow around a cylinder curves around the surface due to the force normal to the surface. This can be integrated as an equivalent side force in the lateral direction, which cannot be expressed by the single actuator drag line model.

2.5.2 Multiple Actuator Lines Model with Drag and Side Forces

To deflect the streamlines around the cylinder, an intuitive idea comes to mind that two equal-and-opposite forces can be added in the lateral direction. This method is developed using the knowledge from the classical potential-flow solution to the non-rotating cylinder flow. In the potential theory of a non-rotating cylinder, there are no lift and drag forces acting on the cylinder overall. But if the cylinder is axially cut in half, the integration of the pressure distribution along the surface of a semi-circle will give a side force that can deflect streamlines. Two semi-circles have the same magnitude of the side force but in the opposite direction, so the total effect is zero. To model this effect without violating this constraint, the side forces are placed off the center in the lateral direction.

So globally, the drag effect is accomplished by the drag line in the tower center with the force projection being the same as the single actuator drag line model. Two additional actuator lines work on deflecting the flow streamlines around the tower. The magnitude of the side force is determined by the side force coefficient, and the flow speed is sampled at the center of the actuator point. Using the exact solution to the non-rotating cylinder flow in potential theory, the reference value for the side force coefficient is found. It is the integration of the pressure coefficient along the surface of a semi-circle in potential flow.

$$C_s = -\int_0^{\pi} (1 - 4\sin^2\theta)\sin\theta d\theta = \frac{10}{3} \tag{2-21}$$

As for the single actuator drag line model, the side forces at each actuator point are also projected onto the flow field with a simple three-dimensional Gaussian function. For the multiple actuator lines with drag and side forces, four parameters can be varied; they are the drag coefficient, C_d, side force coefficients, C_s, the placement of the side force relative to the drag force, Δy, and the force projection width, ε.

2.5.3 Actuator Line with Cp-Based Force Distribution Model

The idea for this model was proposed by Dr. Matthew J. Churchfield [32] and inspired by the viscous pressure distribution around a non-rotating cylinder, see Figure 2-10(c). Generally, the force acting on the cylinder surface can be decomposed into the forces that act normal to the surface and shear stresses that act tangential to the surface. Considering the normal force only, the direction of the forces at each point is aligned with the radial line from the tower center, which suggests the force is a function of the local azimuth angle, θ. Unlike the single actuator drag line model or multiple actuator lines model with drag and side forces, which project the integrated forces over the cylinder surface, a new projecting function is created for the actuator line with the Cp-based force distribution model to spread the force only on the cylinder shell region that is coincident with the tower wall. The projection function is given by

$$g(r,\theta,z) = C\exp[-(\frac{z - z_0}{\varepsilon_z})^2]\exp[-(\frac{r - R}{\varepsilon_r})^2] \tag{2-22}$$

where C is a constant given by

$$C = \{\pi^{3/2}\varepsilon_z\varepsilon_r^2 \exp[-(\frac{R}{\varepsilon_r})^2] + \pi^2\varepsilon_z\varepsilon_r R[1+\mathrm{erf}(\frac{R}{\varepsilon_r})]\}^{-1} \quad (2\text{-}23)$$

The cylindrical coordinates are centered on the tower axis, and R is the tower section radius. The Gaussian spreading widths are defined as $\varepsilon_r = \varepsilon_z = \varepsilon$ .The total drag force is specified by the drag coefficient, C_d, and the sampled velocity. The velocity for the actuator line with Cp-based force distribution model is measured upstream of the tower instead of at the tower center. A force distribution function is created to mimic the experimental measurements at the respective Re_D, which is shown in Figure 2-11. One should note that the shape of the distribution function is also a function of the Reynolds number, Re_D. Integrating the distributed normal force in the drag direction, the desired drag force is recovered.

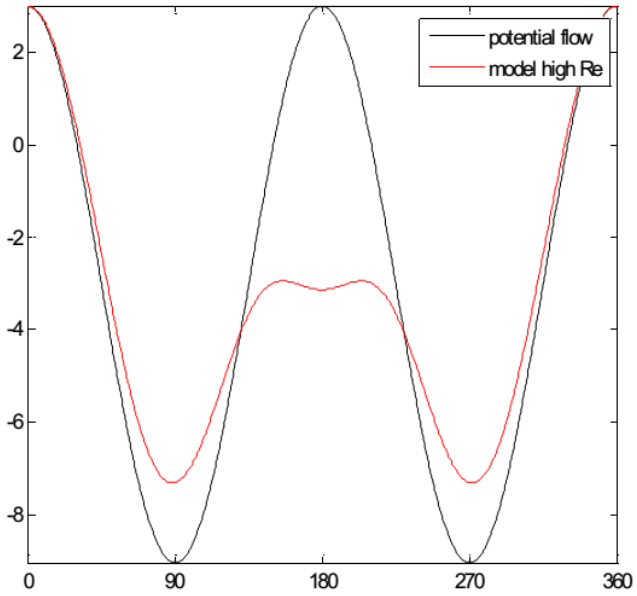

Figure 2-11. Force distribution along non-rotating cylinder (tower) [32].

The force distribution function is given as

$$g(\theta) = (g_{potential} + g_{correction}) / 1.0416\pi \quad (2\text{-}24)$$

where

$$g_{potential} = 1 - 4\sin^2(\theta) \tag{2-25}$$

is the pressure distribution from the potential solution, and

$$g_{correction}(\theta) = 1 - 3\exp[-(\frac{\theta-\pi}{\pi/4})^2] - \exp[-(\frac{\theta-\pi}{\pi/4})^2]\exp[-(\frac{\theta-2\pi}{\pi/2})^2] \tag{2-26}$$

is the correction function to account for viscous effects. It mainly changes the pressure distribution at the rear part of the circle to account for a steady separated region. The scale factor ensures that the integral of the body force in the axial direction recovers the desired drag at an average tower Reynolds number of 2×10^5.

The parameters that can be varied for this model are the Gaussian spreading width, ε, the drag coefficient, C_d, and the most important one, the assumed shape of the force distribution function $g(\theta)$.

Chapter 3 Results and Discussion

In this section, simulation results for the NREL Phase VI rotor with implementation of the three tower models are discussed and compared with experimental data. The first operating condition is a 7m/s uniform wind speed with zero degree yaw. Parametric studies are performed with the single actuator drag line model and multiple actuator lines model with drag and side forces. For the actuator line with Cp-based force distribution model, testing conditions are extended to wind speeds of 7m/s with 10º and 20º yaw, 9m/s with 10º yaw, and 5m/s with 10º yaw as summarized in Table 3-1. The results compared here are the normal force, tangential force, and axial force at 5 radial location, i.e. 30%, 47%, 63%, 80%, 95% of the blade span. The aerodynamic force definitions are shown in the Figure 3-1. The simulation uses 24 million cells with the finest grid resolution of about 0.1367m near the turbine rotor and tower. The simulation time for each case is 10 seconds of real time using 128 processors with a time step of 0.0017361 second. At a constant rotor RPM of 72, which means that a total of 2 rotor revolution are modeled.

Table 3-1. Summary of simulation settings for NREL Phase VI Rotor.

U_w (m/s)	Yaw Angle (degree)		
	0	10	20
5	C	C	C
7	S,M,C	C	C
9	C	C	C

(S-Single actuator drag line model, M-Multiple actuator lines model with drag and side forces, C- Actuator line with Cp-based force distribution model)

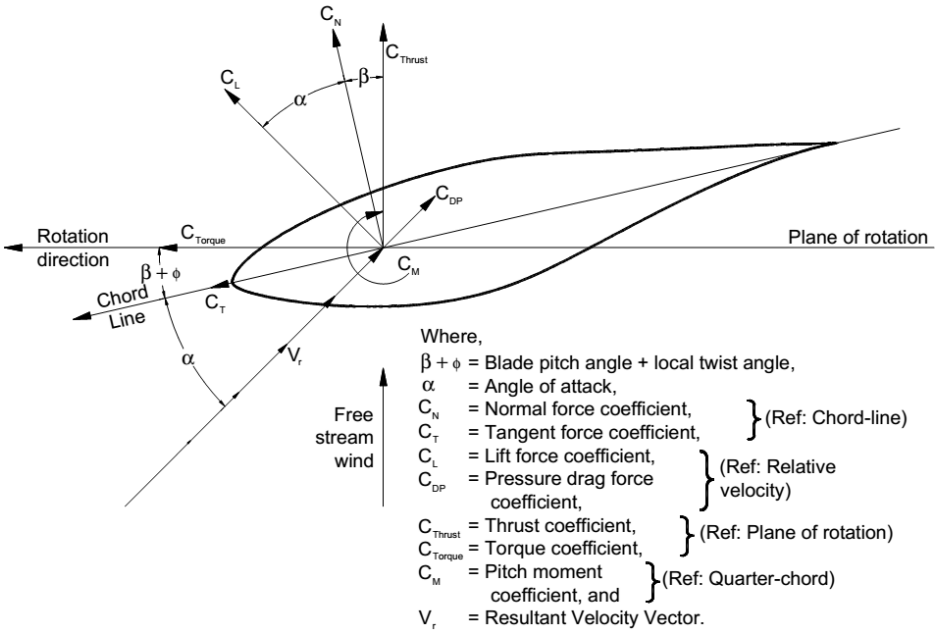

Figure 3-1. Aerodynamic force coefficient definition (NREL Phase VI Rotor) [23].

3.1 Single Actuator Drag Line Model

The single actuator drag line model is first used to account for the tower effect. Here the body-force projection function is the standard three-dimensional Gaussian distribution where the tower is modeled as a single parked actuator line with zero lift and a constant drag coefficient of $C_d = 0.5$ and 1. Figure 3-2 shows the baseline comparison of phased-averaged normal and tangential force distribution along the blade between NREL data and the ALM simulation with and without implementation of the single actuator drag line model. The Gaussian spreading width is $\varepsilon = 4\Delta x$. These result shows that the implementation of the tower model has a very small effect on the mean force value. This is expected; however, the main effects of a tower are to contribute to blade fatigue,

which is important to be quantified, and to alter the wake flow field, which has effects on the wake recovery process.

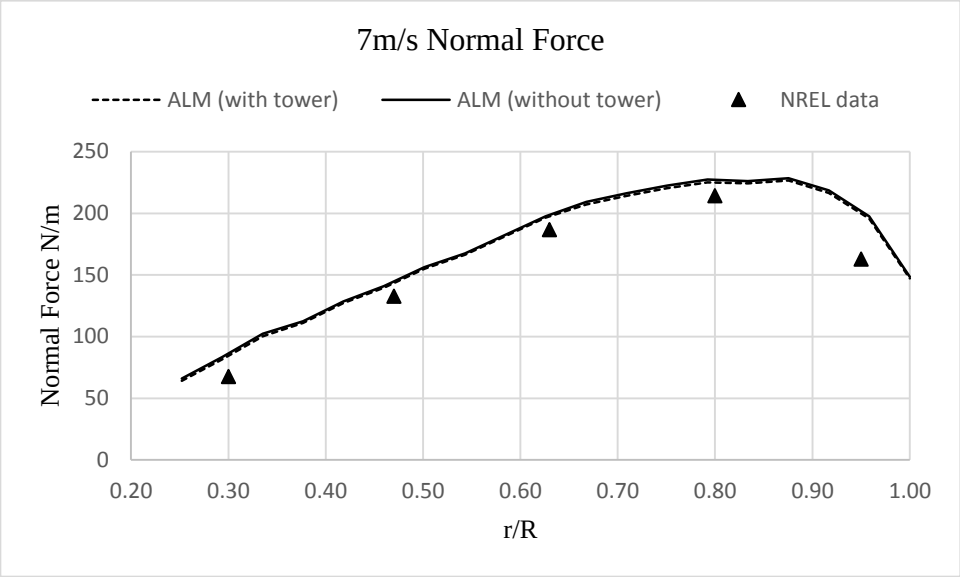

(a)

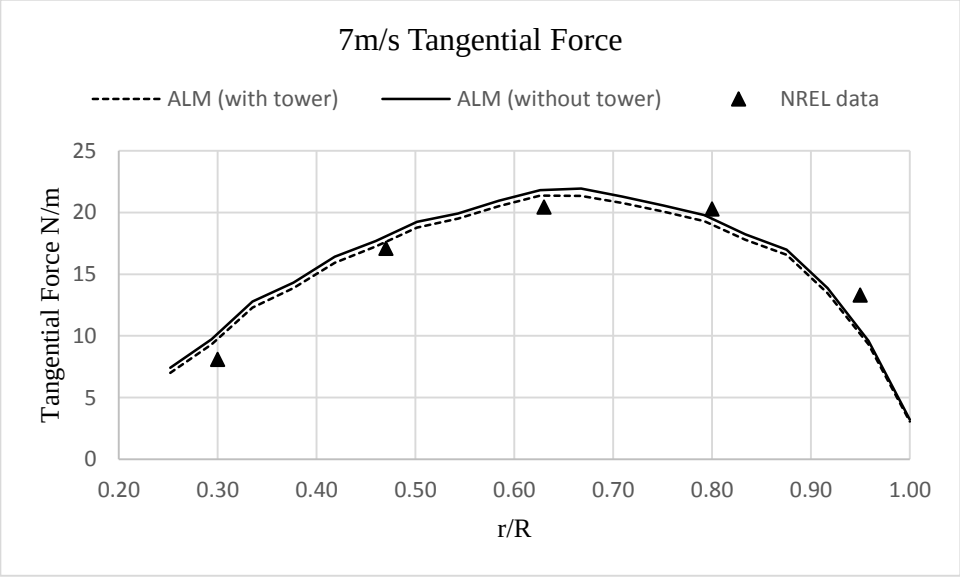

(b)

Figure 3-2. Spanwise distribution of normal and tangential force using single actuator drag line model (NREL Phase VI Rotor, V_{wind} = 7m/s, zero yaw).

The computational results in Figure 3-3 show the decrease in normal force, tangential force, and axial force as the blade passes in front of the tower. It is clear that the magnitude and width of the region affected by the tower strongly depends on the Gaussian spreading width, ε, and drag coefficient, C_d. As the Gaussian spreading width increases, the decrease in the axial force is reduced, which is attributed to a larger, though weaker, volumetric body-force projection. As a result, the region of axial induction becomes larger with less strength. A lower drag coefficient of $C_d = 0.5$ shows an improved agreement with measured data; however, as discussed in the cylinder-flow review, the drag coefficient of the non-rotating circular cylinder is primarily a function of Reynolds number. The turbine tower diameter in the blade-tower interaction region is about 0.4m, hence the Reynolds number is about 1.9×10^5, which suggests that $C_d = 1$ is a reasonable choice with reference to Figure 3-3. In addition, it is clear that by using drag-only actuators to represent the tower, the flow appears to pass through the tower rather than being deflected by the solid boundary. As shown in Figure 3-4, the flow also does not experience strong deceleration upstream of the tower, nor does it create a large flow deflection around the tower.

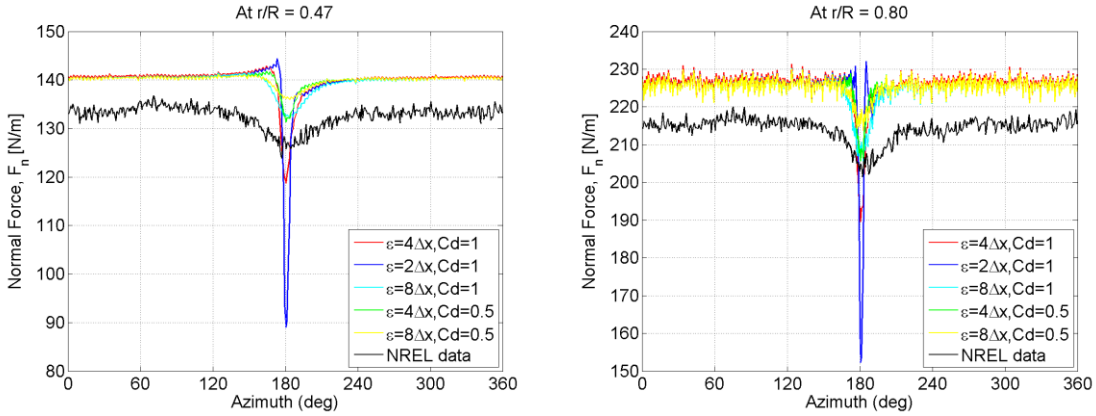

(a)

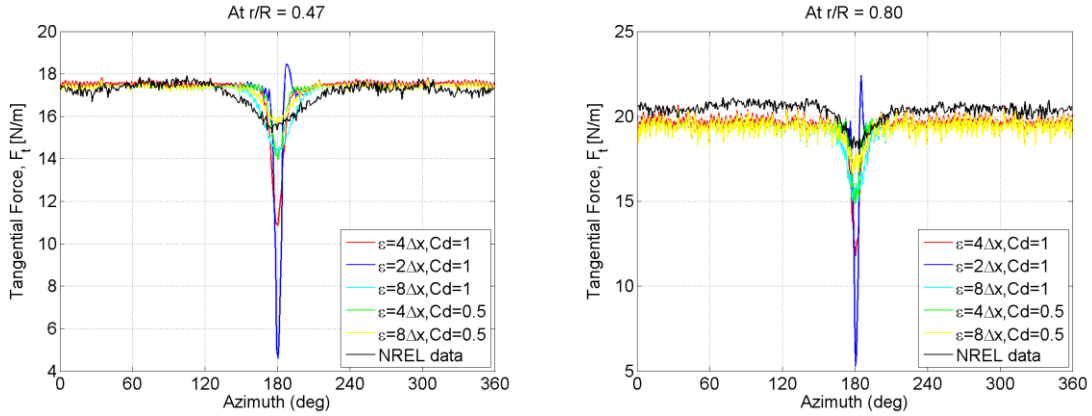

(b)

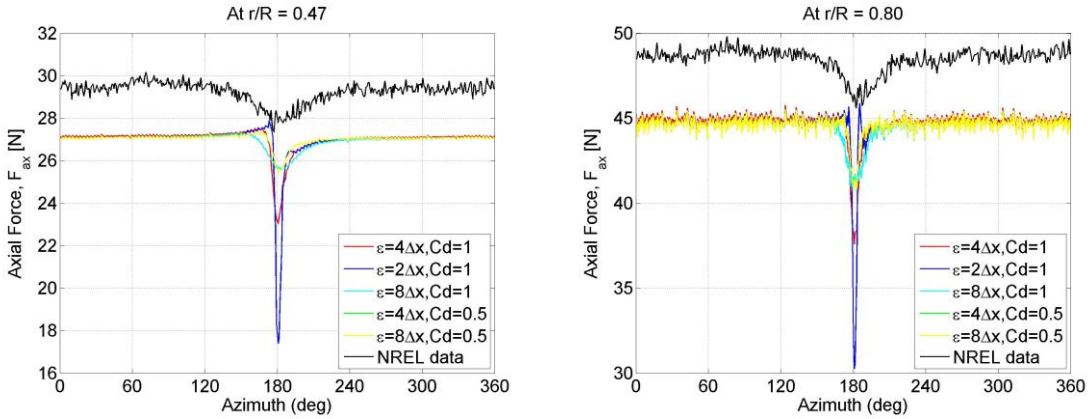

(c)

Figure 3-3. Phase-averaged blade loads (Single Actuator Drag Line Model) (a) Normal force (b) Tangential force (c) Axial force (NREL Phase VI Rotor, V_{wind} = 7m/s, zero yaw).

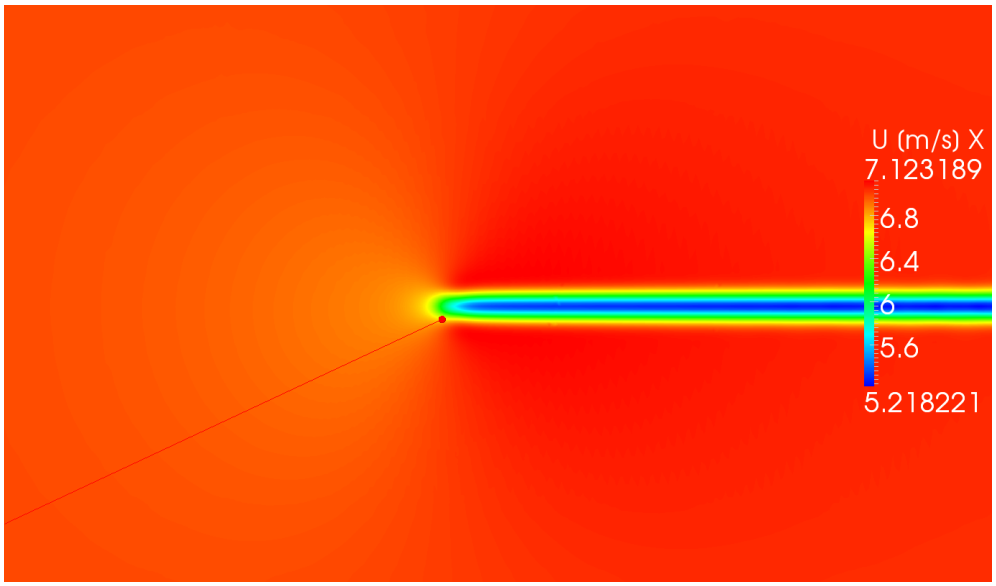

(a)

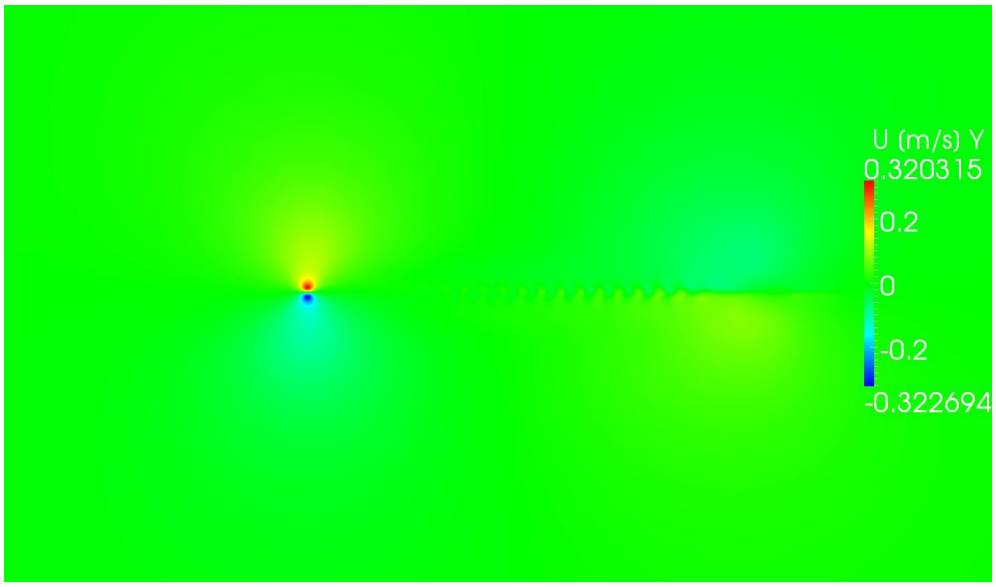

(b)

Figure 3-4. (a) Axial velocity and (b) lateral velocity near tower using the single actuator drag line model (NREL Phase VI Rotor, V_{wind} = 7m/s, zero yaw).

3.2 Multiple Actuator Lines Model with Drag and Side Forces

An improvement to the tower model was inspired by classical potential flow around a cylinder. A non-rotating cylinder has no lift force generated overall as the flow is symmetric, but the streamlines deflect and contract along the axial direction. It is clear that the flow deflection around the tower is important for an upwind wind turbine since the turbine blade actually passes through a flow region where streamlines are affected by the presence of the tower. An intuitive way to model this effect is adding a pair of side forces to the actuator line of equal-and-opposite strength pointing outward (normal to the axial flow) to create streamline curvature (or deflection) around the tower. Using the same three-dimensional Gaussian function to project the equal-and-opposite side forces, unlike the lifting line (or drag line in this case), the side-force actuator lines need to be placed off the center line to avoid direct cancellation. Figure 3-5 shows a baseline comparison of phased-averaged normal and tangential force distribution along the blade between NREL data and ALM simulation with and without implementation of multiple actuator lines with drag and side forces. Here the side force location is chosen as $\Delta y = \Delta x$ with a Gaussian spreading width of $\varepsilon = 4\Delta x$.The spanwise location of the side force lines is explored in addition to the Gaussian spreading width, ε.

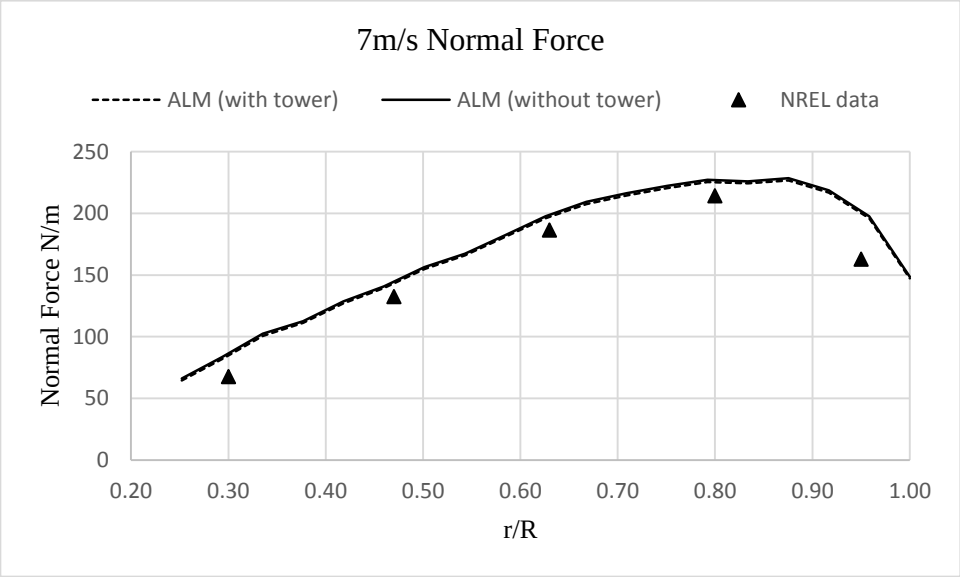

(a)

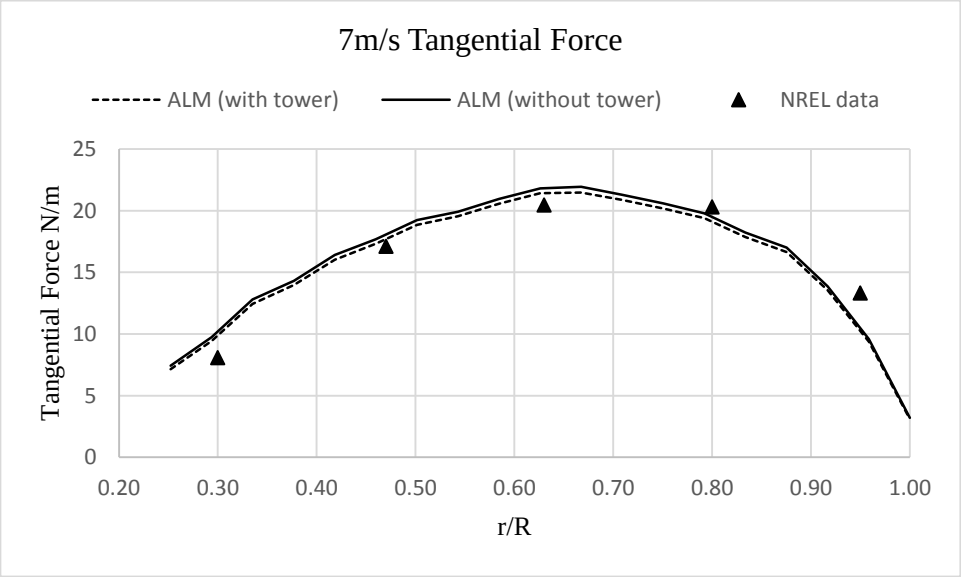

(b)

Figure 3-5. Spanwise distribution of normal and tangential force using multiple actuator lines model with drag and side forces (NREL Phase VI Rotor, V_{wind} = 7m/s, zero yaw).

Table 3-2. Side force location parametric variation for tower model using multiple actuator lines model with drag and side forces ($\varepsilon = 4\Delta x$).

	Positon in the *y* direction (m)
1	$\Delta y = 2\Delta x$
2	$\Delta y = \Delta x$
3	$\Delta y = 0.5\Delta x$
4	$\Delta y = 0.25\Delta x$

Next, the magnitude of the side forces needs to be determined. From knowledge of potential flow around the non-rotating cylinder, one can obtain a first-order estimate of the upper/lower lift coefficient. By splitting the tower axially into two equal semi-circles, one obtains two highly-cambered airfoils. By integrating the exact pressure distributions along the semi circles, one finds a virtual lift coefficient of C_l =10/3 =3.33, see equation (2-21). Although there exists flow separation on the rear of the tower (cylinder) in the real world, which reduces the virtual lift coefficient estimated from the exact potential-flow solution, it is still a reasonable estimation and step ahead to building an improved tower model.

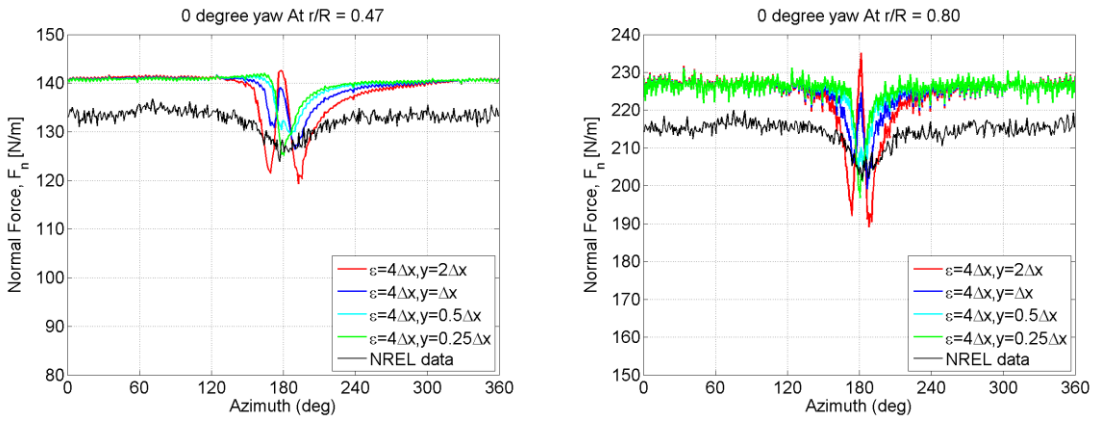

(a)

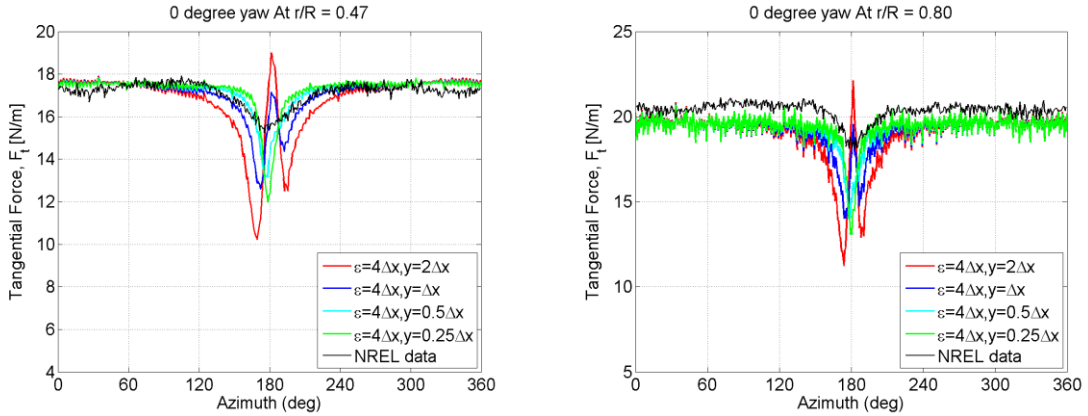

(b)

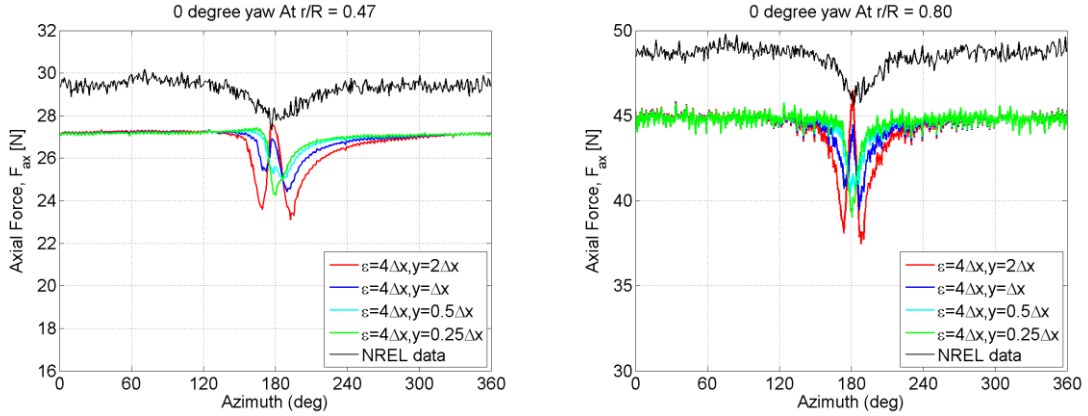

(c)

Figure 3-6. Phase-averaged blade loads with different side location, Δ*y* (Multiple Actuator Lines Model with Drag and Side Forces) (a) Normal force (b) Tangential force (c) Axial force (NREL Phase VI Rotor, V_{wind}=7m/s, zero yaw).

The initial consideration about the side-force location was placing it $\Delta y = 2\Delta x$ away from the tower in the lateral direction so that the distance between the two actuator-line centers representing the side forces is close to the tower diameter, which can be regarded as an upper limit of the location. As shown in Figure 3-6, after applying the side forces, the axial-force reduction region is expanded and the peak is reduced, both effects are as desired. By moving the side force close to the tower center, the width of this region shrinks, and the axial-force reduction is enhanced when reaching 180º. As stated above, the multiple actuator lines with drag and side forces degrades to a simple drag tower when the distance between the side forces goes to zero. Unexpectedly, there is a

reverse peak that lies in the reduction region whose width and strength is reduced as the side forces move closer to each other. Since the side forces have equal-and-opposite strengths, they nearly cancel each other close to the tower centerline. The gap, however, creates a free path (or jet) through the tower that is not affected by the deflection. Based on the axial-force result shown in Figure 3-6, $\Delta y = 0.5\Delta x$ provides a good match to experimental data while encountering a small reverse-peak flow.

In the preliminary computational result for the simple actuator drag line model, it was found that by increasing the Gaussian projection width, ε, the axial-force reduction controls the peak load as the blade passes in front of the tower. This makes the region of axial induction due to the tower drag larger, but of less strength. For the multiple actuator lines model with drag and side forces, the effect of the Gaussian projection width, ε, on the computational result is studied next, with a side-force location of $y = 0.5\Delta x$ and a Gaussian spreading width, ε, of $4\Delta x$, $6\Delta x$, and $8\Delta x$, as shown in Table 3-3.

Table 3-3. Gaussian spreading width parametric variation using multiple actuator lines model with drag and side forces ($\Delta y = 0.5\Delta x$).

	Gaussian spreading width(ε)
5	$\varepsilon = 4\Delta x$
6	$\varepsilon = 6\Delta x$
7	$\varepsilon = 8\Delta x$

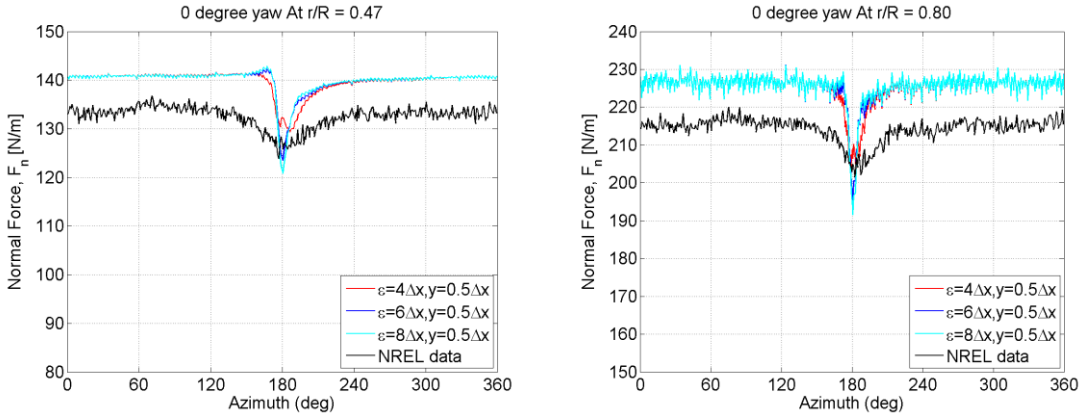

(a)

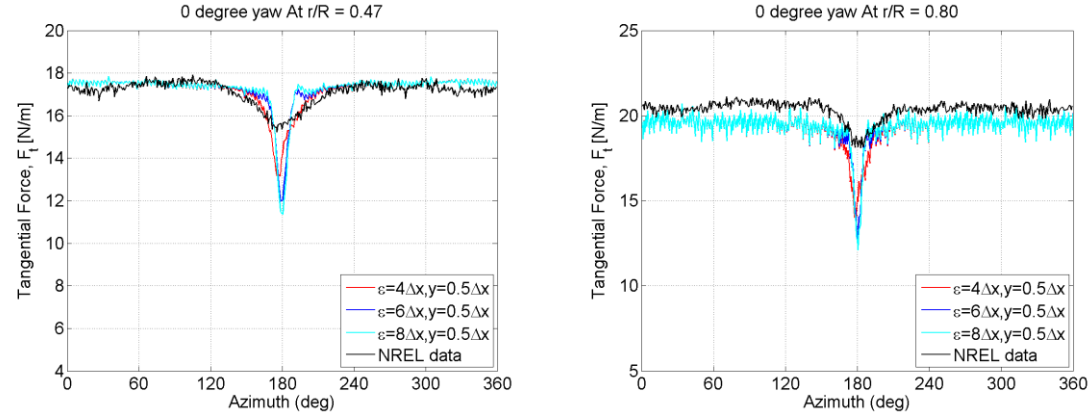

(b)

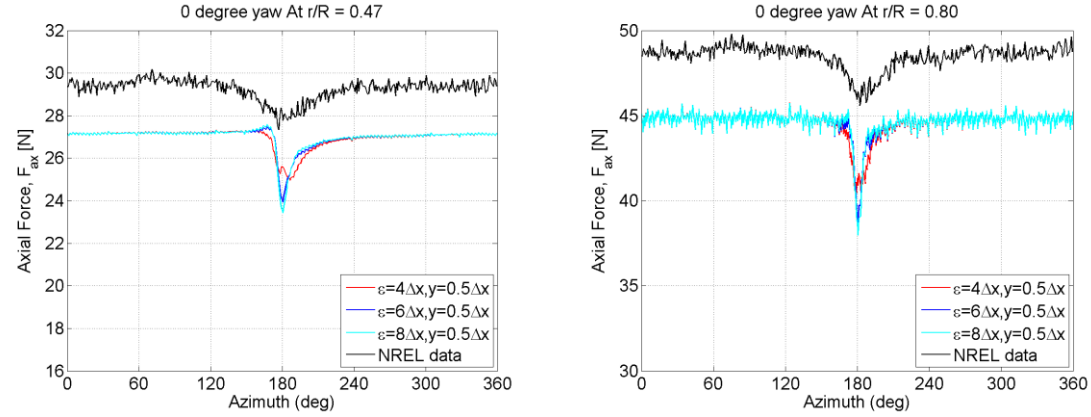

(c)

Figure 3-7. Phase-averaged blade loads with different Gaussian width, ε. (Multiple Actuator Lines Model with Drag and Side Forces) (a) Normal force (b) Tangential force (c) Axial force (NREL Phase VI Rotor V_{wind}=7m/s, zero yaw).

As shown in Figure 3-7, increasing the Gaussian projection width, ε, helps smoothing the reverse-load region but it also narrows the reduction region and reduces the peak load at the same time. This is because each side force is more dominant on its own side and thus contracts the central free-path region. This proves that streamline deflection plays an important role in upwind wind-turbine unsteady blade loads. In conclusion, adding a side force in addition to the simple actuator drag line model improves the prediction of the axial blade load by expanding the axial-force reduction region and reducing the peak compared to the result of the simple actuator drag line model. The placement of the side force and the chosen Gaussian spreading width, ε, have a profound impact on its response.

3.3 Actuator Line with Cp-based Force Distribution Model

The performance of the actuator line with Cp-based force distribution model is discussed in this section. The computational results for the baseline case (V_{wind} = 7m/s, zero yaw) of the normal force, tangential force, and axial force are shown in Figure 3-8.

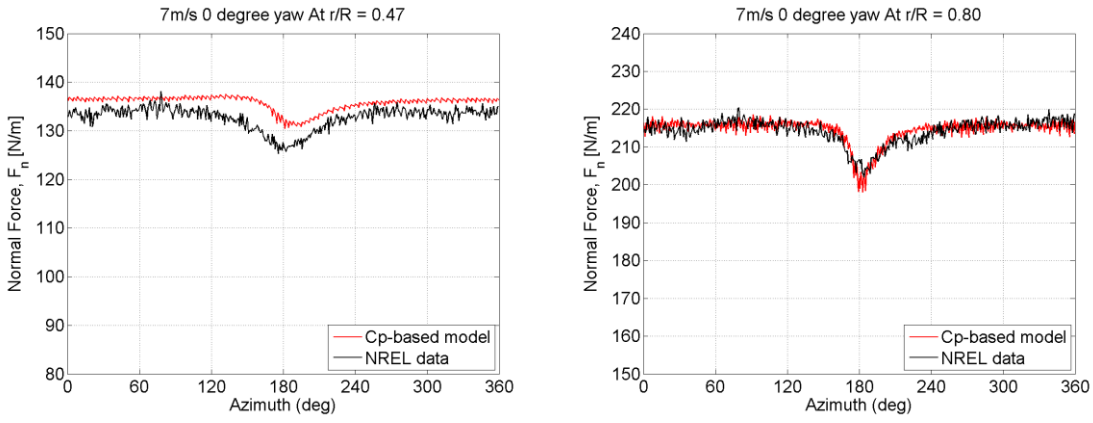

(a)

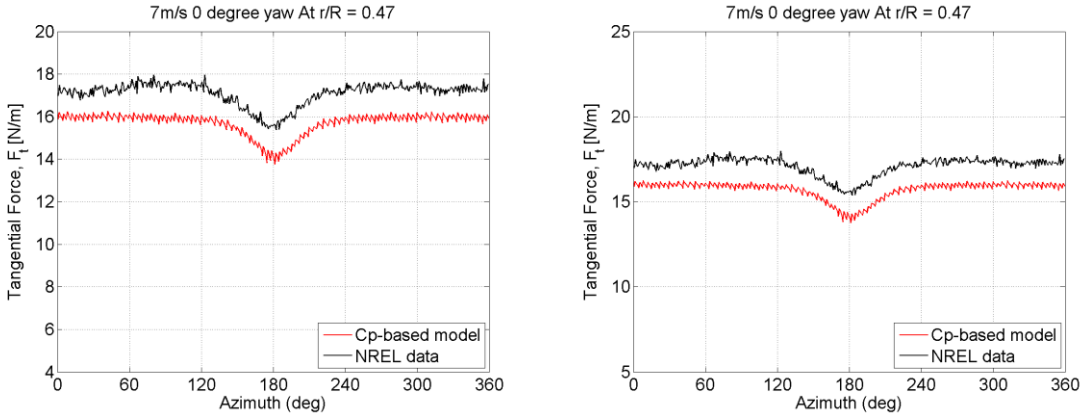

(b)

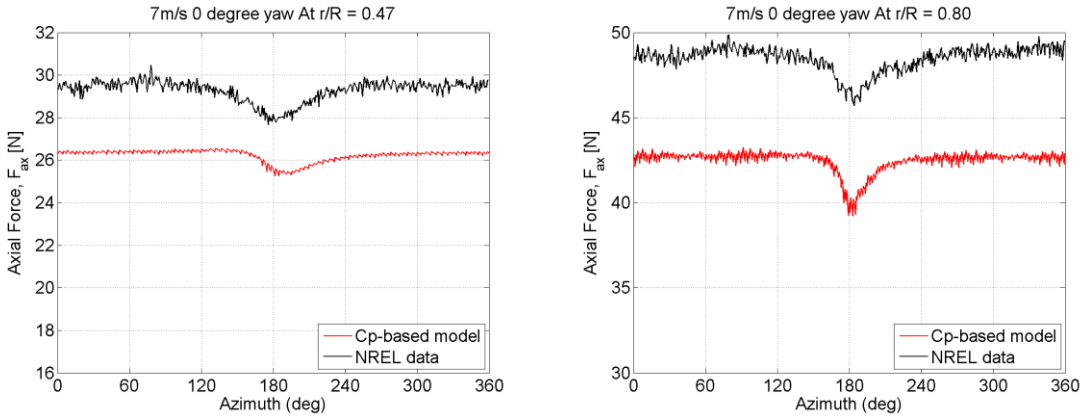

(c)

Figure 3-8. Phase-averaged blade loads (Actuator Line with Cp-based Force Distribution Model) (a) Normal force (b) Tangential force (c) Axial force (NREL Phase VI Rotor, V_{wind}=7m/s, zero yaw).

Compared with the mean force offset, the reduction magnitude, azimuthal width and shape of the single actuator drag line model in Figure 3-3 and multiple actuator lines model with drag and side forces in Figure 3-6, the actuator line with Cp-based force distribution model shows a better performance with respect to blade load prediction.

3.3.1 Effect of Turbine Yaw

In a steady yaw condition, the flow field is more complex for the rotating blade because the sectional inflow conditions vary with azimuth, even without blade-tower interaction. Figure 3-9 shows the blade loads at 10º yaw and Figure 3-10 shows the blade load at 20º yaw, both at 7m/s wind speed. It can be seen that the blade load prediction captures the load changes due to steady yaw and blade-tower interaction both at the inboard location, i.e. *r/R* = 47%, and the outboard location, i.e. *r/R* = 80%. When the yaw angle is increased to 20º, the NREL data show that the azimuthal variation of blade loads becomes more pronounced, but the actuator line with a Cp-based force distribution model stills works quite well.

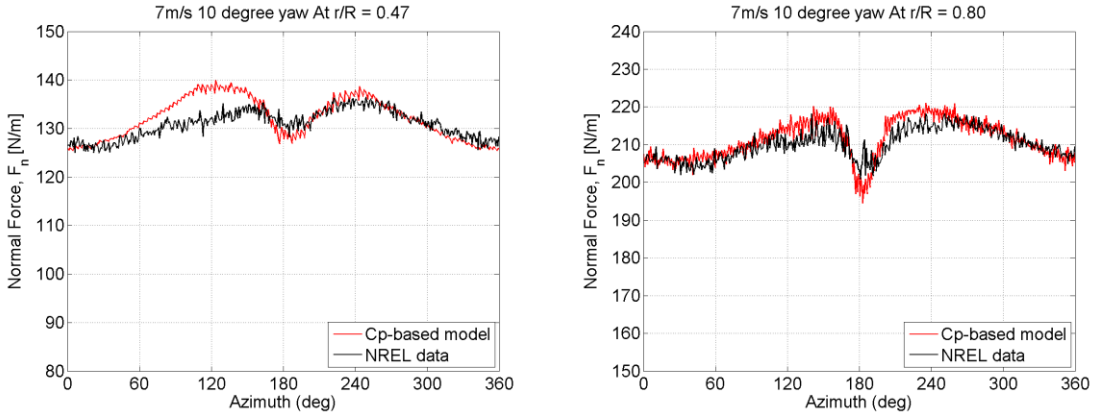

(a)

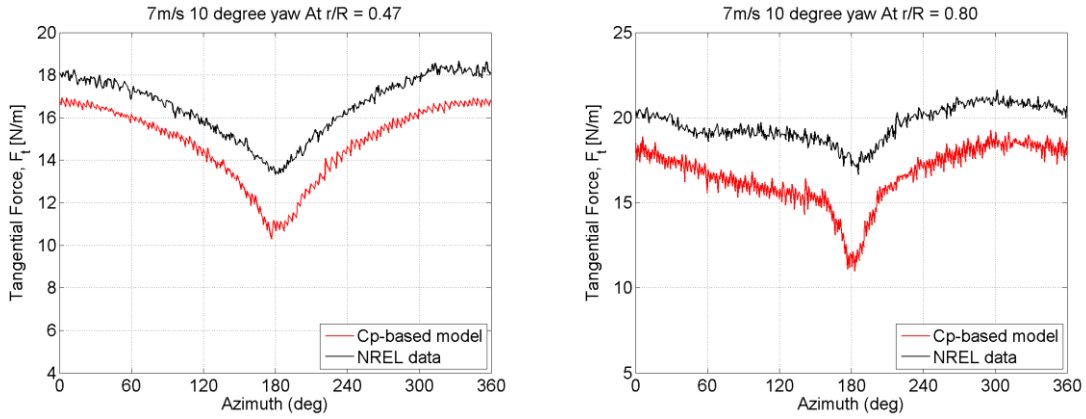

(b)

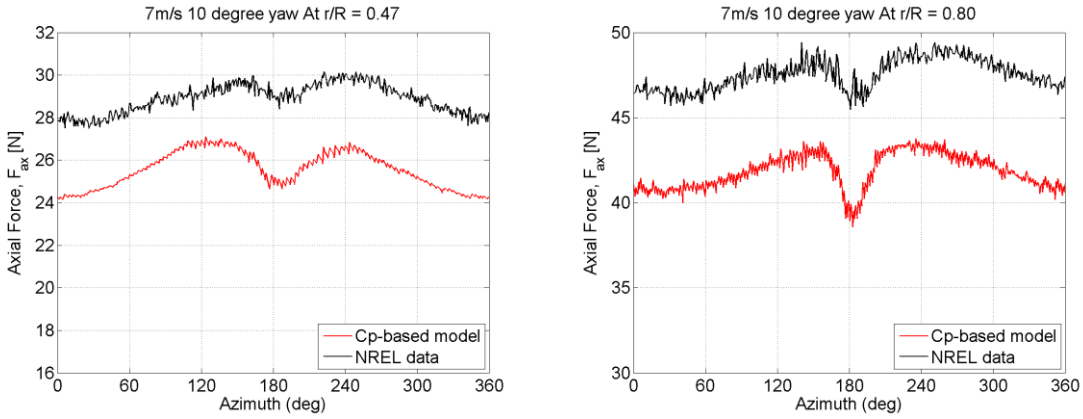

(c)

Figure 3-9. Phase-averaged blade loads (Actuator Line with Cp-based Force Distribution Model) (a) Normal force (b) Tangential force (c) Axial force (NREL Phase VI Rotor, V_{wind}=7m/s, 10° yaw).

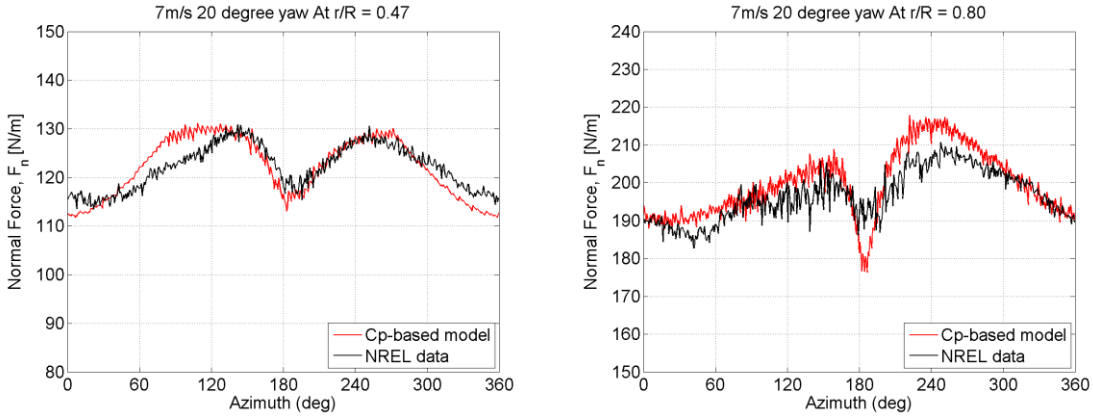

(a)

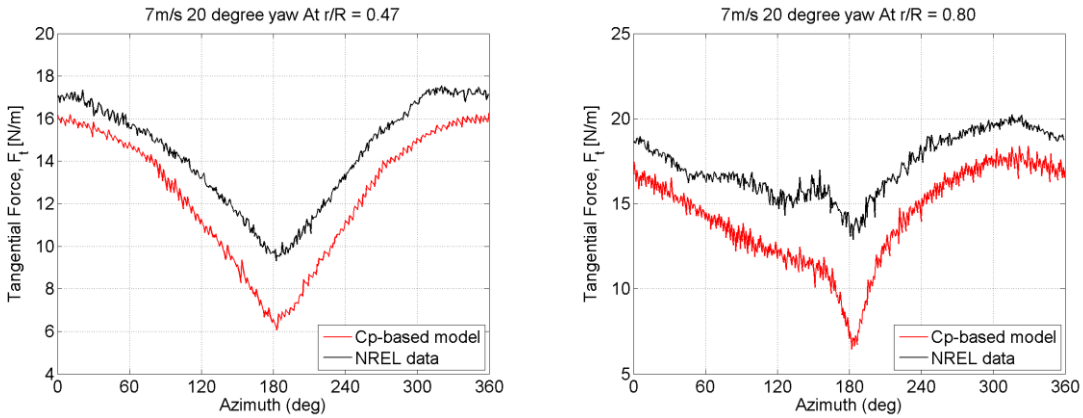

(b)

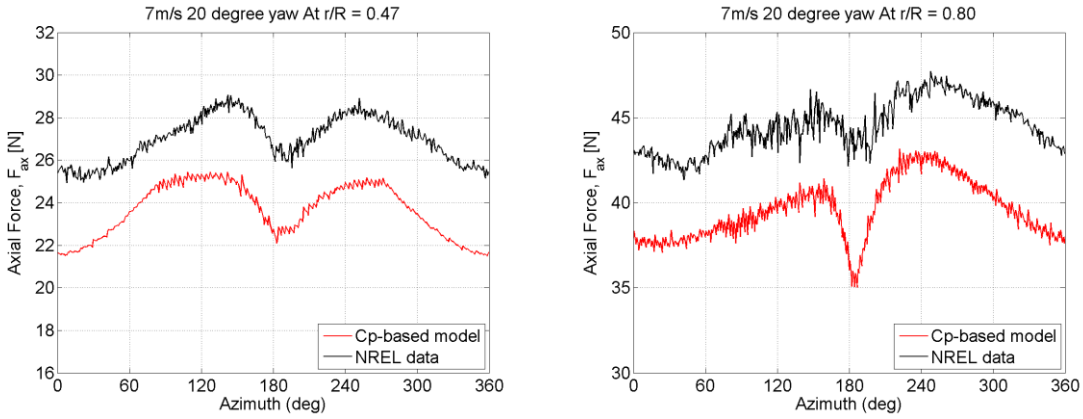

(c)

Figure 3-10. Phase-averaged blade loads (Actuator Line with Cp-based Force Distribution Model) (a) Normal force (b) Tangential force (c) Axial force (NREL Phase VI Rotor, V_{wind}=7m/s, 20° yaw).

3.3.2 Effect of Wind Speed

In addition to steady yaw conditions, the actuator line with the Cp-based force distribution model is also tested at different incoming wind speeds. Since the rotor RPM stays the same at 72, a change in wind speed corresponds to a change in TSR (tip speed ratio). A higher TSR at 5m/s uniform wind speed and a lower TSR with 9m/s uniform wind speed is chosen here. From the Figure 3-11, it is difficult to see a strong force reduction in the interacting region from NREL data at the inboard location *r/R* = 47%. The mean force offset between the actuator line with a Cp-based force

distribution model and NREL data is also much larger compared to previous cases at this location, while it is small at the outboard location. It is possible that the inboard part of the blade is stalled in that condition, which is difficult to capture by the ALM method. At higher TSR, as shown in Figure 3-12, the actuator line with Cp-based force distribution model works as expected.

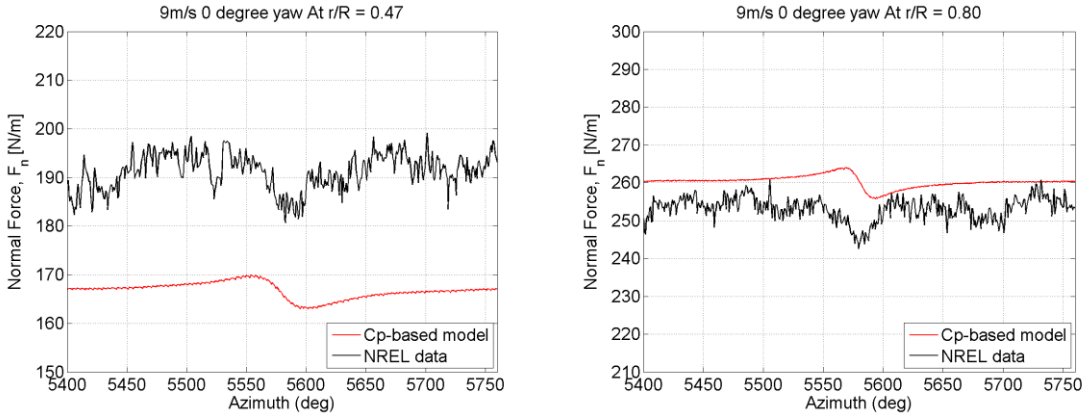

(a)

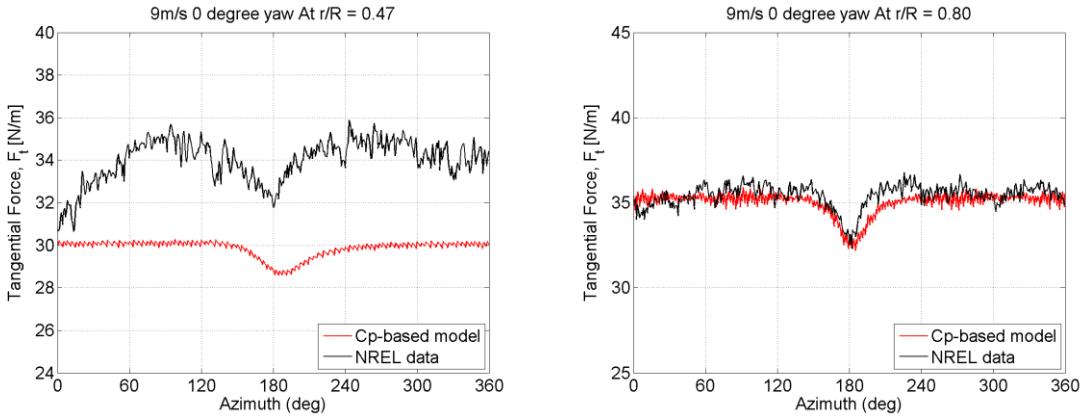

(b)

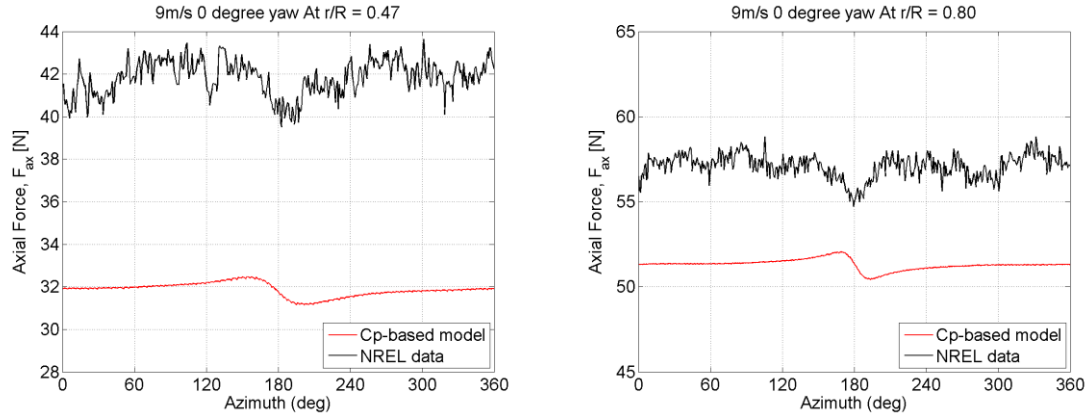

(c)

Figure 3-11. Phase-averaged blade loads (Actuator Line with Cp-based Force Distribution model) (a) Normal force (b) Tangential force (c) Axial force (NREL Phase VI Rotor, V_{wind} = 9m/s, zero yaw).

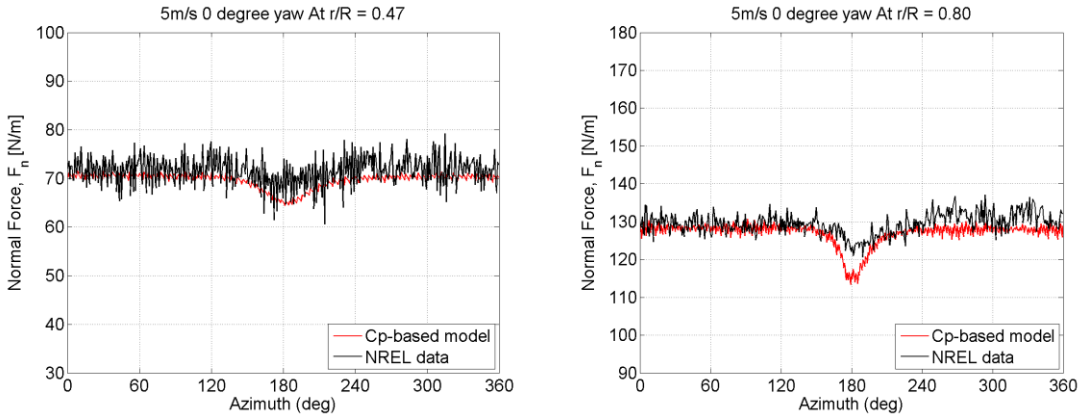

(a)

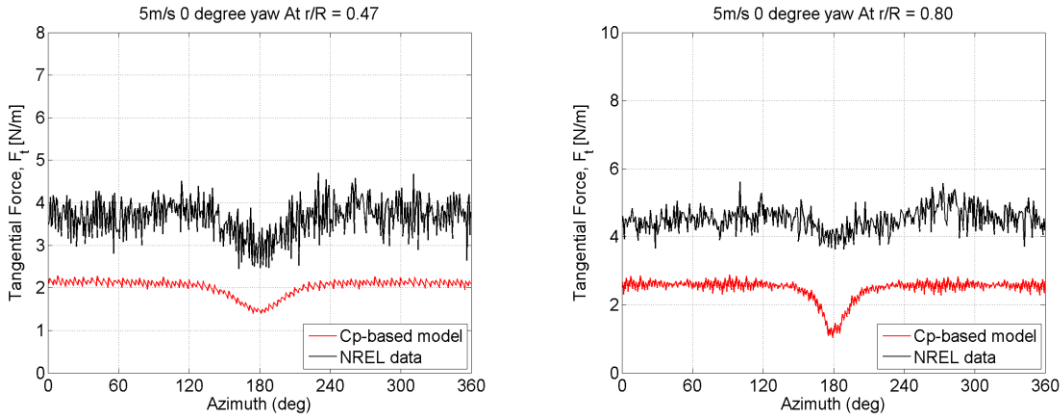

(b)

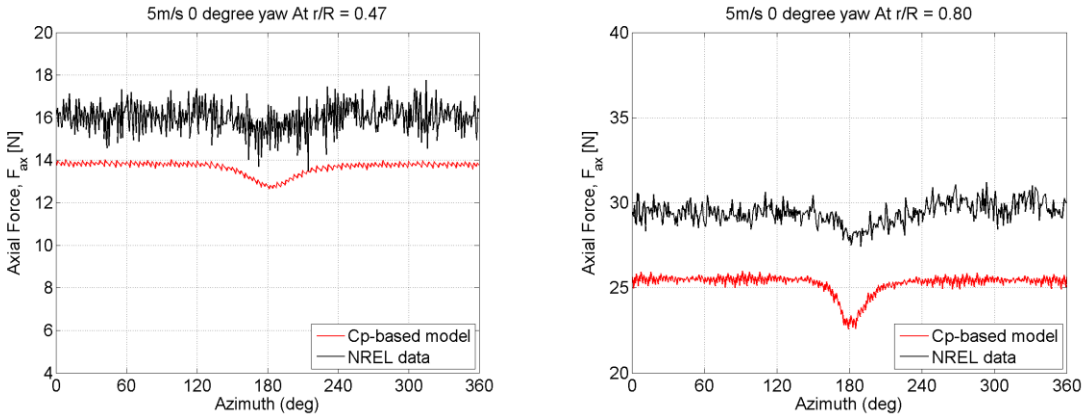

(c)

Figure 3-12. Phase-averaged blade loads (Actuator Line with Cp-based Force Distribution model) (a) Normal force (b) Tangential force (c) Axial force (NREL Phase VI Rotor, V_{wind} = 5m/s, zero yaw).

Table 3-4 shows the phase-averaged value comparison of the rotor thrust force and power between NREL test data and ALM simulation results (without and with tower model). From the ALM simulation results, it can be seen the implementation of the tower model still slightly reduces the total power and thrust force, and the changes lie within 2%. Figure 3-13, 3-14, and 3-15 show the phase-averaged value of normal force and tangential force at five radial locations along the blade ,5m/s, 7m/s, and 9m/s. It is also observed that, although the force reduction is quite an obvious phenomenon varying with azimuth angle, the tower effect on the mean force value is limited.

Table 3-4. Comparison of measured NREL data and ALM simulations with and without tower (NREL Phase VI Rotor).

	NREL test		ALM(without tower)		ALM(with tower)	
wind speed(m/s)	Thrust (N)	Power(kw)	Thrust(N)	Power(kw)	Thrust(N)	Power(kw)
5	681.78	2.02	692.83	2.04	686.31	2.01
7	1149.50	6.03	1232.90	5.81	1224.20	5.73
9	1507.20	10.37	1513.00	9.40	1538.40	9.36

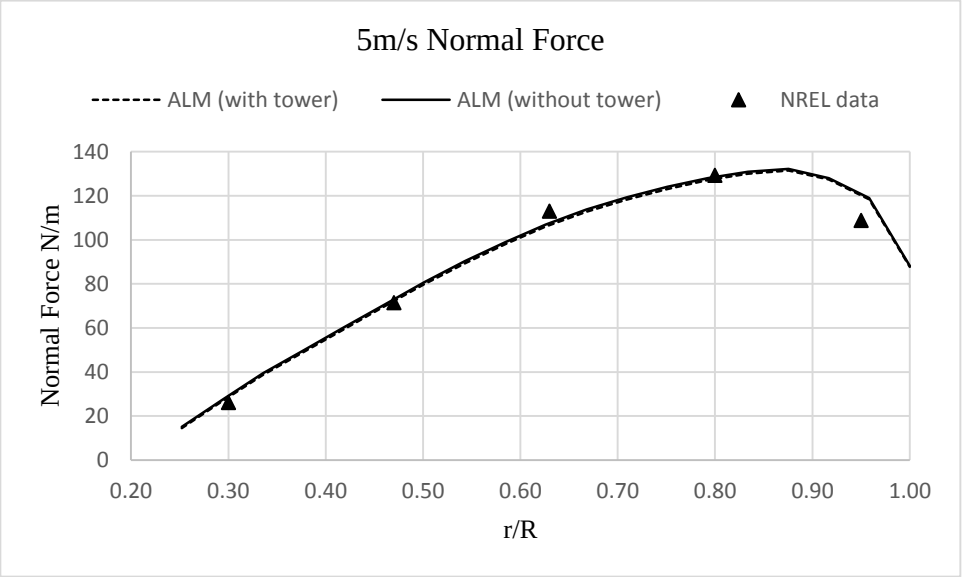

(a)

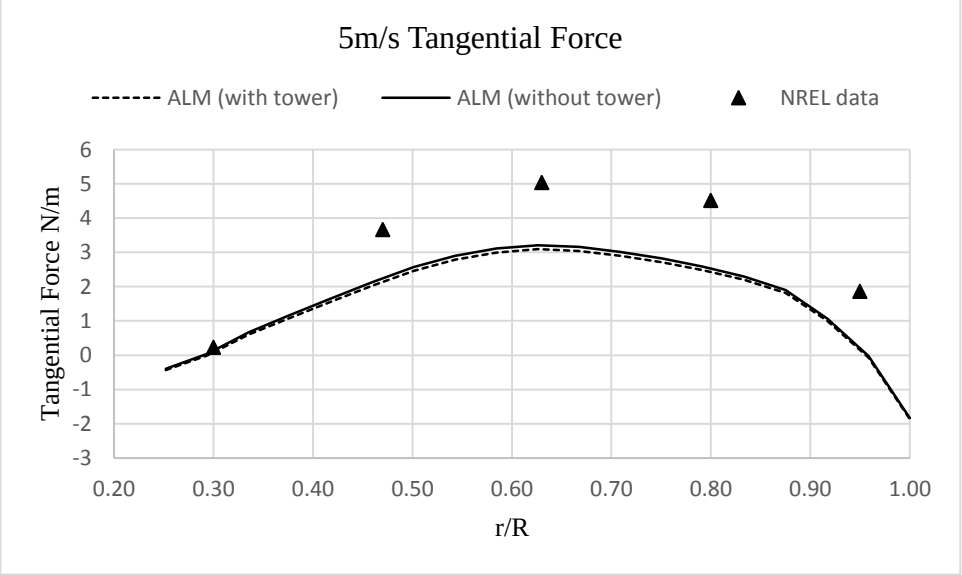

(b)

Figure 3-13. Spanwise distribution of normal and tangential force using actuator line with Cp-based force distribution model (NREL Phase VI Rotor, V_{wind} = 5m/s, zero yaw).

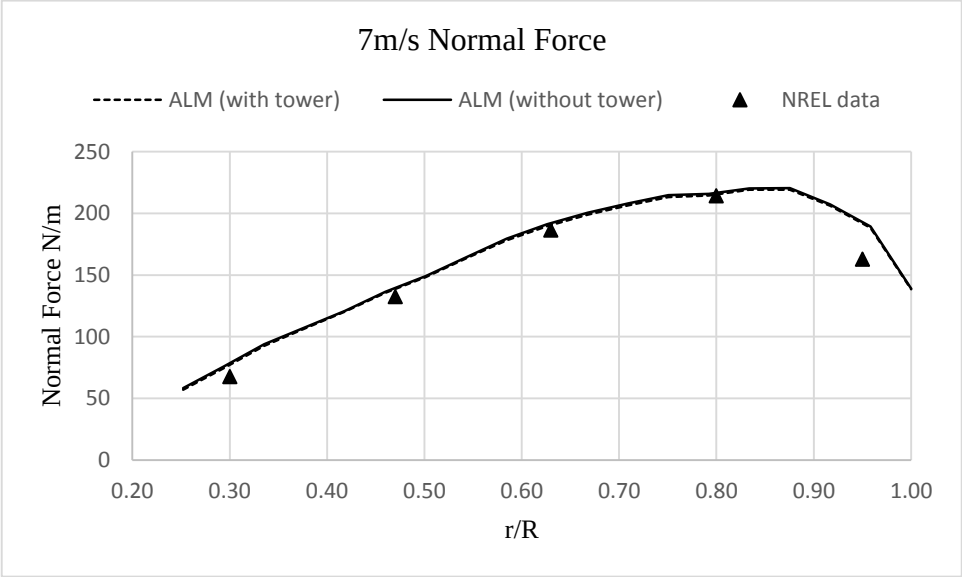

(a)

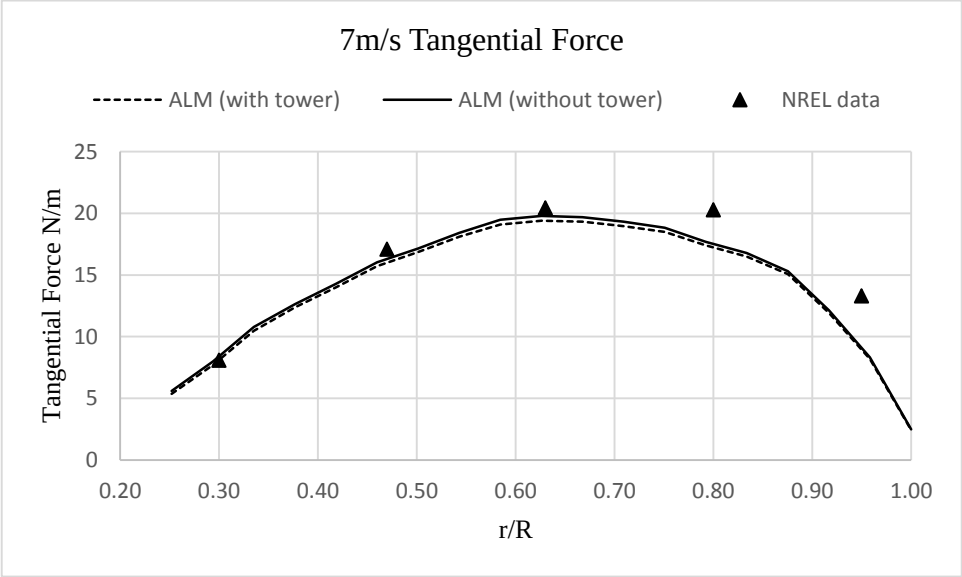

(b)

Figure 3-14. Spanwise distribution of normal and tangential force using actuator line with Cp-based force distribution model (NREL Phase VI Rotor, V_{wind} = 7m/s, zero yaw).

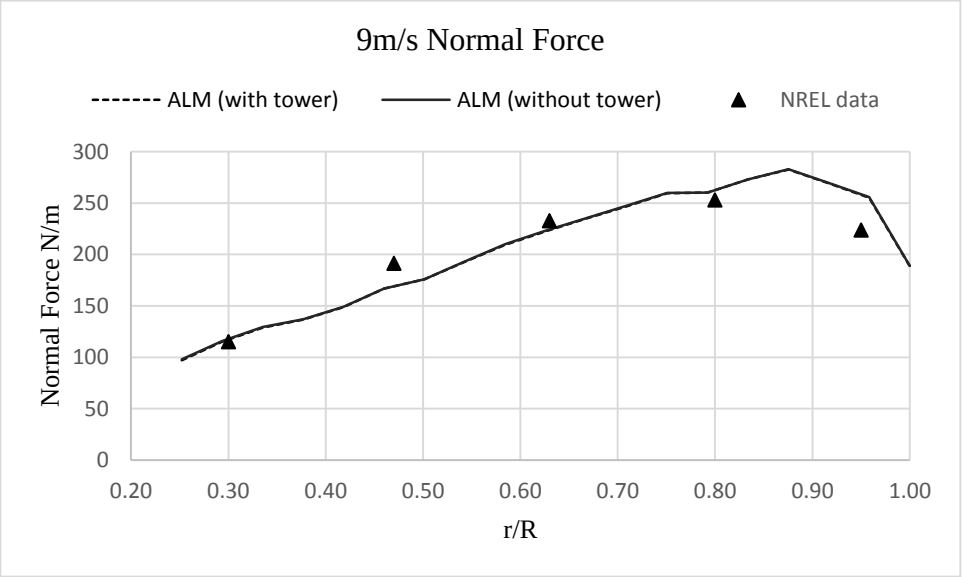

(a)

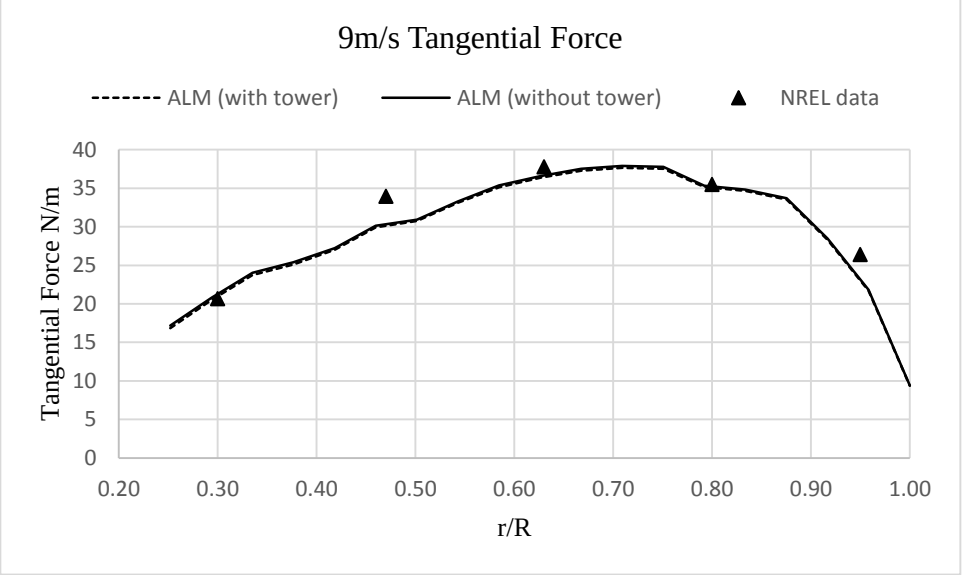

(b)

Figure 3-15. Spanwise distribution of normal and tangential force using actuator line with Cp-based force distribution model (NREL Phase VI Rotor, V_{wind} = 9m/s, zero yaw).

A final set of simulations combines the different wind speeds and steady yaw angles, namely 9m/s with 10° yaw and 5m/s with 10° yaw. Figure 3-16 shows the blade load with the wind turbine operating at 10° yaw with a 9m/s uniform wind speed.

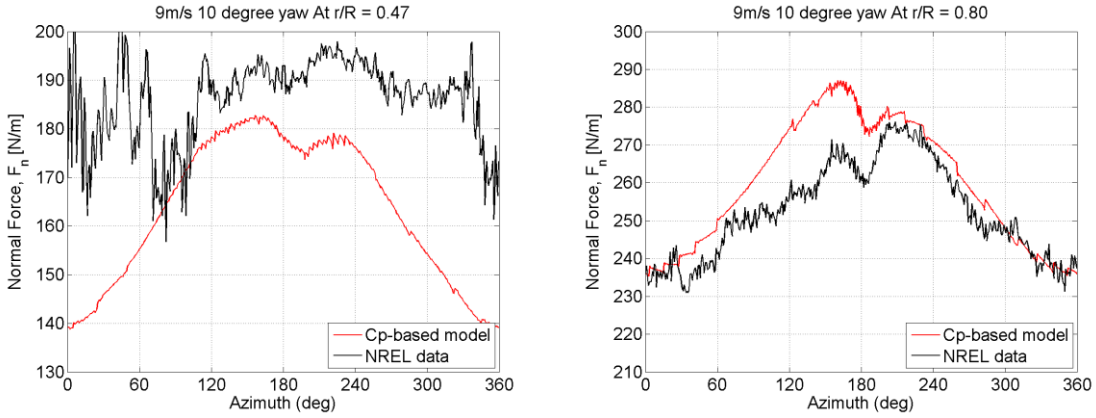

(a)

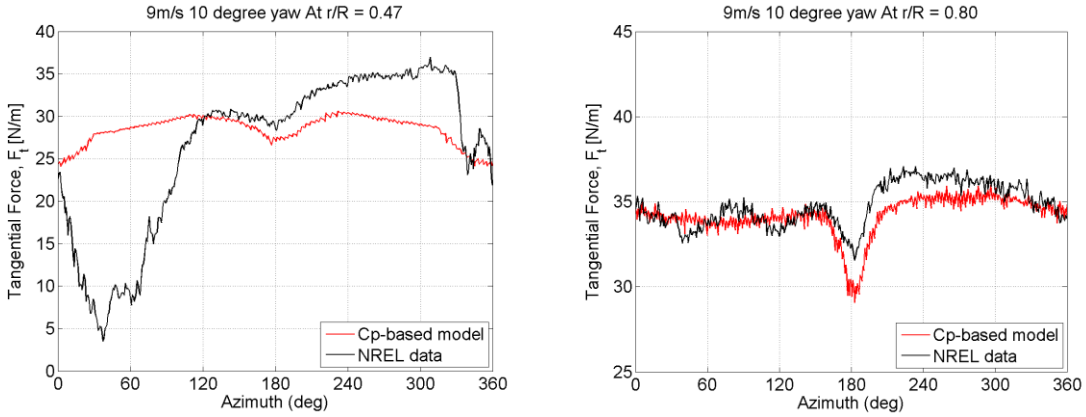

(b)

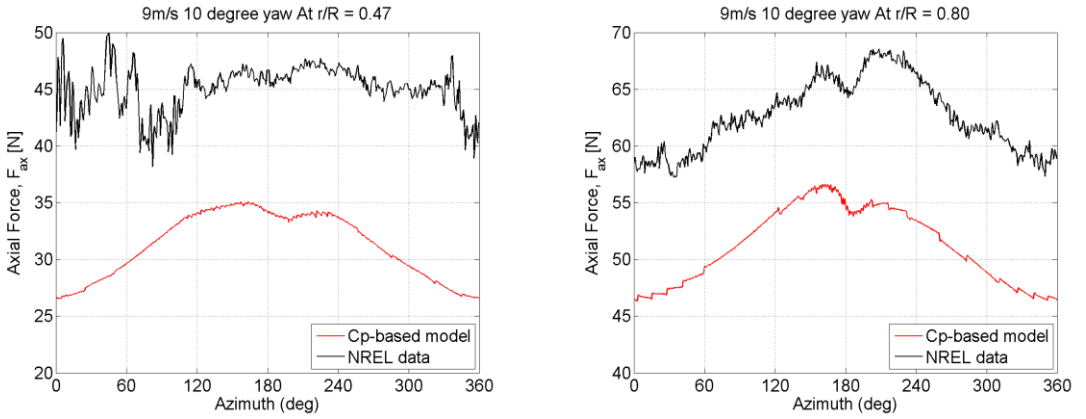

(c)

Figure 3-16. Phase-averaged blade loads (Actuator Line with Cp-based Force Distribution Model) (a) Normal force (b) Tangential force (c) Axial force (NREL Phase VI Rotor, V_{wind} = 9m/s, 10° yaw).

Figure 3-16 shows the blade load with the wind turbine operating at 10º yaw with 5m/s uniform wind speed.

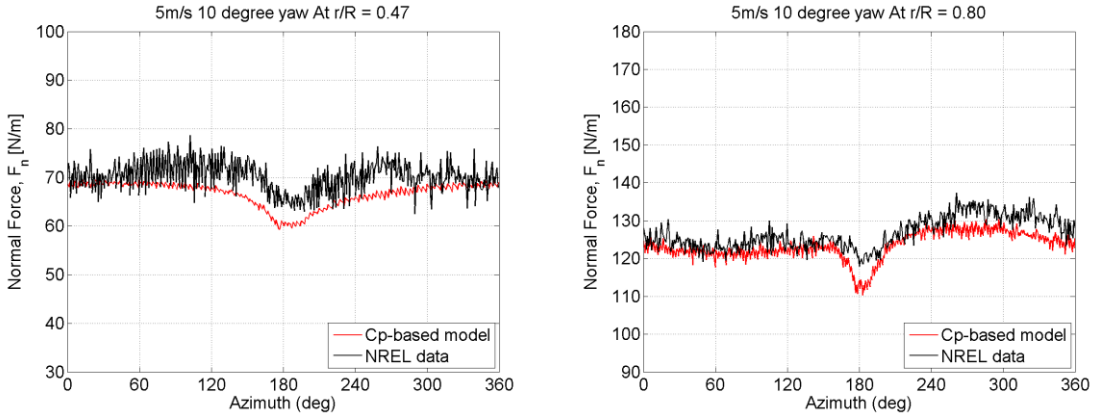

(a)

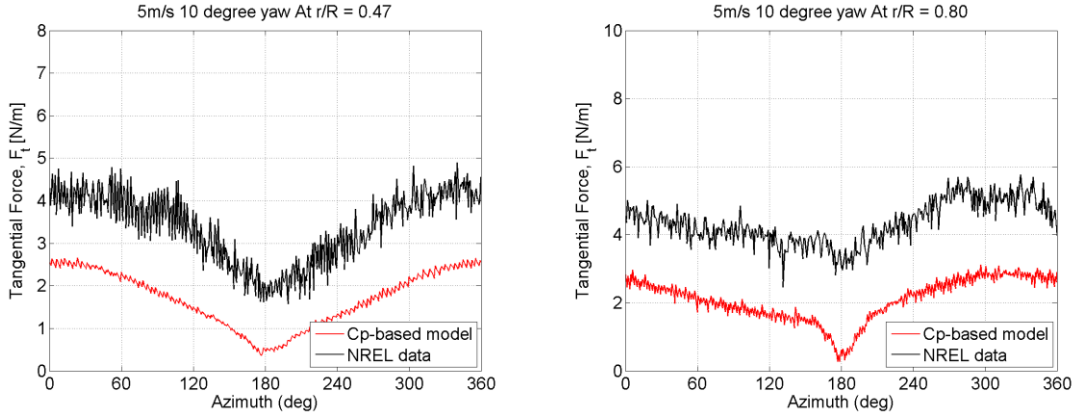

(b)

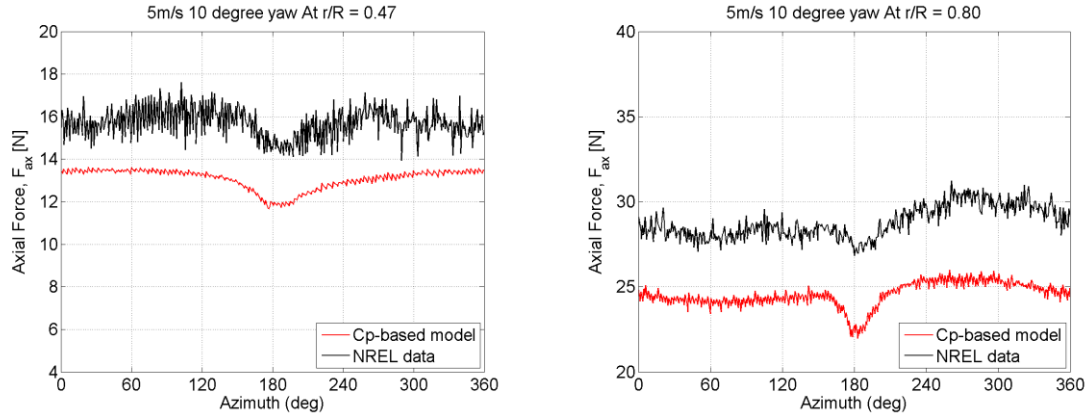

(c)

Figure 3-17. Phase-averaged blade loads (Actuator Line with Cp-based Force Distribution Model) (a) Normal force (b) Tangential force (c) Axial force (NREL Phase VI Rotor, V_{wind} = 5m/s, 10° yaw).

It is interesting to see that for the higher TSR (5m/s), the simulation prediction is still good, while for the lower TSR (9m/s), the simulation result hardly matches the NREL data at the 47% inboard location, which can be expected from the 9m/s zero-yaw case. When the incoming wind velocities increases, the inflow angle is increased along the blade and so is the local angle of attack. The inboard part of the blade always operates at a higher angle of attack than the outboard part and is more sensitive to the change in incoming wind speed. The yaw condition also makes a contribution when the blade moves towards the incoming wind. The asymmetric shape of the experimental data at 47%R of the blade in Figure 3-16 shows that separation occurs. As stated in previous discussions, the ALM uses a 2D airfoil lookup table and projects the chordwise distributed force as an integrated lift and drag force, which makes it difficult to capture separation and stall.

Chapter 4 Conclusions

Wind turbine wake modeling using the actuator line method (ALM) is becoming increasingly important in the wind energy community. Besides a lot of progress in the field, an efficient actuator-type method to include tower interference effects has been missing to date. A tower model is important to study its effect on the time-varying blade loads and the wake recovery process.

In this thesis, three different tower models named i) single actuator drag line model, ii) multiple actuator lines model with side and drag forces and iii) actuator line with Cp-based force distribution model are developed using the body-force method, specifically, the actuator line method (ALM). All three models are implemented in the NREL Phase VI rotor model in OpenFOAM. Computed results include the sectional blade loads projected as normal force, tangential force, and axial force and are compared to measured data at 5 radial location along the turbine blade. The goal is to develop a tower model with the body-force method that is general enough to be applied to different operating conditions and different yaw angles. This will improve the accuracy of large wind farm simulations by including the tower effect with little penalty on the computational cost.

From the results, it is observed that the single actuator drag line model and multiple actuator lines model with drag and side forces achieve some success in the blade load prediction, but the parametric study suggests that results highly depend on the selected parameters such as Gaussian width, ε, drag coefficient, C_d, and lateral location, Δy.

The actuator line with Cp-based force distribution model, however, gives more promising performance predictions. As shown in comparison plots against measured data, the blade load predictions from the actuator line with Cp-based force distribution model are more accurate both in magnitude and shape in the tower interference region. When separation occurs at the inboard

blade part at low TSR or large yaw angle, the method fails to capture the experimental result due to the assumption of static airfoil data. But this is more a limitation of ALM of the rotor model rather than the effect of the tower model. In conclusion, the actuator line with Cp-based force distribution model is a good engineering model accounting for the tower effects with low computational cost and has the potential to be used in large wind farm simulations by researchers in the wind energy community.

Future Work

It has been shown in this thesis study that the actuator line with Cp-based force distribution model shows good performance in blade load predictions at various operating conditions. Some further improvements can be made for the tower model in future work.

As discussed in the cylinder flow review, the pressure distribution around the tower, mainly at the rear part, changes with time particularly at high Reynolds number. For the NREL Phase VI wind turbine operating at 7m/s, there exists a dominant frequency with $St = 0.2$ vortex shedding at this Reynolds number. This information can be used to change the steady force distribution to model the unsteady behavior. Although such time variation is not expected to make a big difference in the blade loads because the integrated drag force only changes by about 10% due to the tower shadow. Such variation and oscillating frequency play a role, though, in the turbine wake, which is important in large wind farm simulations.

In addition, the force distribution used for the simulations in this work is based on a single fixed Reynolds number [33]. To be general, a force distribution needs to be developed as a function of Reynolds number or a look up table such that the code will automatically choose the one based on the inflow condition and initial setting.

References

[1] Righter, R. W., 1996, *Wind Energy in America: A History*, University of Oklahoma Press, Norman, pp. 46.

[2] Rivkin, D. A., Randall, M., and Silk, L., 2011, *Wind Power Generation and Distribution*, Jones & Bartlett Publishers, Burlington,VT, pp. 3.

[3] Logan, J., Kaplan, S. M., 2008, "Wind Power in the United States: Technology, Economic, and Policy Issues," CRS Report for Congress, pp. 12.

[4] Schmitz, S., 2014, "Wind Turbines Then and Now," *Wind Turbine Aerodynamics*, https://www.e-education.psu.edu/aersp583/

[5] http://www.windpower.org/pictures/lacour.htm (Last accessed: July 9th).

[6] Hansen, M. O., 2008, *Aerodynamics of wind turbines*, Earthscan, NY, pp. 28.

[7] Manwell, J. F., McGowan, J. G., and Rogers, A. L., 2010, *Wind Energy Explained, Theory, Design, and Applications*, John Wiley & Sons., NY, pp. 96.

[8] Manwell, J. F., McGowan, J. G., and Rogers, A. L., 2010, *Wind Energy Explained, Theory, Design, and Applications*, John Wiley & Sons., NY, pp. 100.

[9] Schmitz, S., and J. J. Chattot., 2006, "A Coupled Navier-Stokes/Vortex-Panel Solver for the Numerical Analysis of Wind Turbines," *Computers and Fluids*, **35** (7), pp. 742-745.

[10] Munduate, X., Coton, F. N., and Galbraith, R. A. M., 2004, " An Investigation of the Aerodynamic Response of a Wind Turbine Blade to Tower Shadow*," Journal of Solar Energy Engineering*, **126**(4), pp. 1034-1040.

[11] Leishman, J. G., 2006, *Principles of Helicopter Aerodynamics*, Cambridge University Press, NY, pp. 760.

[12] http://mstudioblackboard.tudelft.nl/duwind/Wind energy online reader/ Static_pages/ upwind_ downwind.htm (Last accessed: July 9th).

[13] Mittal, R., Iaccarino, G., 2005, "Immersed Boundary Methods," *Annu. Rev. Fluid Mech*, **37** pp. 239-261.

[14] Jha, P. K., Churchfield, M. J., Moriarty, P. J., & Schmitz, S., 2014, "Guidelines for volume force distributions within actuator line modeling of wind turbines on large-eddy simulation-type grids," *Journal of Solar Energy Engineering*, **136**(3), pp. 1-11.

[15] OpenFOAM, 2012, ESI Group-OpenCFD, Ver. 2.0.x, http:// www.openfoam.org/git.php (Last accessed: July 9th).

[16] Issa, R. I., 1986, "Solution of the Implicitly Discretized Fluid Flow Equations by Operator-Splitting," Journal of Computational Physics, **62**, pp. 40–65.

[17] Rhie, C. M., and Chow W. L., 1983, "Numerical Study of the Turbulent Flow Past an Airfoil with Trailing Edge Separation," AIAA Journal, **21**(11), pp. 1525–1532.

[18] Churchfield, M. J., Lee, S., Michalakes, J., & Moriarty, P. J., 2012, "A Numerical Study of the Effects of Atmospheric and Wake Turbulence on Wind Turbine Dynamics," Journal of Turbulence, **13**(12), pp. 1–32.

[19] Jha, P. K., Churchfield, M. J., Moriarty, P. J., and Schmitz, S., 2013, "Accuracy of State-of-the-Art Actuator-Line Modeling for Wind Turbine Wakes," AIAA- 2013-0608.

[20] Schmitz, S., 2014, "Combining Momentum Theory and BEM Theory through a, a', and Φ", https://www.e-education.psu.edu/aersp583/node/510 (Last accessed: July 9th).

[21] NWTC Information Portal (AirfoilPrep). https://nwtc.nrel.gov/AirFoilPrep. Last modified 19-December-2014; Accessed 23-June-2015.

[22] Schmitz, S., 2014, "Modeling Wind Turbine Wakes - Actuator Line Modeling", https://www.e-education.psu.edu/aersp583/node/579 (Last accessed: July 9th).

[23] Sørensen, J. N., Shen, W. Z., 2002," Numerical Modeling of Wind Turbine Wakes", Journal of Fluids Engineering, **124**(2), pp. 393-399.

[24] Jha, P. K., Churchfield, M. J., Moriarty, P. J., and Schmitz, S., 2013, "Accuracy of State-of-the-Art Actuator-Line Modeling for Wind Turbine Wakes," AIAA-2013-0608.

[25] Schreck, S., Hand, M., & Fingersh, L. J., 2001, "NREL Unsteady Aerodynamics Experiment in the NASA-Ames Wind Tunnel: a Comparison of Predictions to Measurements," NREL/TP-500-29494, National Renewable Energy Laboratory, Golden, CO, USA.

[26] Simms, D. A., Fingersh, L. J., Jager, D. W., Cotrell, J. R., Schreck, S., and Larwood, S. M., 2001, "Unsteady Aerodynamics Experiment Phase VI: Wind Tunnel Test Configurations and Available Data Campaigns," NREL/TP-500-29955, National Renewable Energy Laboratory, Golden, CO, USA.

[27] Spitzer, R. E., 1965, "Measurements of Unsteady Pressures and Wake Fluctuations for Flow over a Cylinder at Supercritical Reynolds Number," Ph.D. thesis, California Institute of Technology, Pasadena, CA, USA.

[28] Relf, E. F., 1914, "Discussion of the Results of Measurements on the Resistance of Wires with Some Additional Tests on the Resistance of Wires of Small Diameter," Rept. Advisory Committee for Aeronautics (ARC Sc.), pp. 102.

[29] Goldstein, S., 1938, *Modern Developments in Fluid Mechanics Vol. II,* Dover Publications, pp. 601-607.

[30] Gerrard, J. H., 1961, "An Experimental Investigation of the Oscillating Lift and Drag of a Circular Cylinder Shedding Turbulent Vortices," **11**(02), pp. 244-256.

[31] Batchelor, G. K., 1967, *An Introduction to Fluid Dynamics*, Cambridge University Press, NY

[32] Roshko, A., 1953, "On the Development of Turbulent Wakes from Vortex Streets," NACA Technical Note 2913, Washington.

[33] Kovasznay, L. S. G., 1949, "Hot-wire investigation of the wake behind cylinders at low Reynolds numbers", In Proceedings of the Royal Society of London A: Mathematical, Physical and Engineering Sciences, **198**, pp. 174-190.

[34] Relf, E. F., and Simmons, L. F. G., 1925, "LIII. On the Frequency of the Eddies Generated by the Motion of Circular Cylinders Through a Fluid", Philosophical Magazine Series, *Series 6*, **49**, pp. 509-511.

[35] Churchfield, M. J., Wang, Z., and Schmitz, S., 2015, "Modeling Wind Turbine Tower and Nacelle Effects within an Actuator Line Model," AIAA-2015-0214.

[36] Aitken, M. L., Kosović, B., Mirocha, J. D., and Lundquist, J. K., 2014, "Large Eddy simulation of Wind Turbine Wake Dynamics in the Stable Boundary Layer Using the Weather Research and Forecasting Model," Journal of Renewable and Sustainable Energy, **6**(3), pp. 033137.

[37] Wu, Y. T., & Porté-Agel, F., 2011, "Large-eddy simulation of wind-turbine wakes: evaluation of turbine parametrisations," *Boundary-Layer Meteorology*, **138** (3), pp. 345-366.